Monthly Notices of the ROYAL ASTRONOMICAL SOCIETY

MNRAS **538,** 1921–1943 (2025) https://doi.org/10.1093/mnras/staf359
Advance Access publication 2025 February 27

JWST meets *Chandra*: a large population of Compton thick, feedback-free, and intrinsically X-ray weak AGN, with a sprinkle of SNe

Roberto Maiolino [1,2,3★] Guido Risaliti,[4,5] Matilde Signorini [5,6] Bartolomeo Trefoloni,[1,4,5] Ignas Juodžbalis [1,2] Jan Scholtz,[1,2] Hannah Übler [1,2] Francesco D'Eugenio [1,2] Stefano Carniani [7] Andy Fabian [8] Xihan Ji [1,2] Giovanni Mazzolari,[9,10] Elena Bertola,[5] Marcella Brusa,[9,10] Andrew J. Bunker,[11] Stephane Charlot [12] Andrea Comastri,[10] Giovanni Cresci,[5] Christa Noel DeCoursey,[13] Eiichi Egami,[13] Fabrizio Fiore,[14,15] Roberto Gilli,[10] Michele Perna,[16] Sandro Tacchella [1,2] and Giacomo Venturi [7]

[1]*Kavli Institute for Cosmology, University of Cambridge, Madingley Road, Cambridge CB3 OHA, UK*
[2]*Cavendish Laboratory – Astrophysics Group, University of Cambridge, 19 JJ Thomson Avenue, Cambridge CB3 OHE, UK*
[3]*Department of Physics and Astronomy, University College London, Gower Street, London WC1E 6BT, UK*
[4]*Dipartimento di Fisica e Astronomia, Università di Firenze, via G. Sansone 1, I-50019 Sesto Fiorentino, Firenze, Italy*
[5]*INAF – Osservatorio Astrofisico di Arcetri, Largo Enrico Fermi 5, I-50125 Firenze, Italy*
[6]*Dipartimento di Matematica e Fisica, Univeristà di Roma 3, Via della Vasca Navale, 84, 00146 Roma RM, Italy*
[7]*Scuola Normale Superiore, Piazza dei Cavalieri 7, I-56126 Pisa, Italy*
[8]*Institute of Astronomy, University of Cambridge, Madingley Road, Cambridge CB3 0HA, UK*
[9]*Dipartimento di Fisica e Astronomia, Università di Bologna, Via Gobetti 93/2, I-40129 Bologna, Italy*
[10]*INAF – Osservatorio di Astrofisica e Scienza dello Spazio di Bologna, Via Gobetti 93/3, I-40129 Bologna, Italy*
[11]*Department of Physics, University of Oxford, Denys Wilkinson Building, Keble Road, Oxford OX1 3RH, UK*
[12]*Institut d'Astrophysique de Paris, Sorbonne Université, CNRS, UMR 7095, 98 bis bd Arago, F-75014 Paris, France*
[13]*Steward Observatory, University of Arizona, 933 N. Cherry Avenue, Tucson, AZ 85721, USA*
[14]*INAF – Osservatorio Astronomico di Trieste, Via G. B. Tiepolo 11, I-34131 Trieste, Italy*
[15]*IFPU – Institut for Fundamental Physics of the Universe, Via Beirut 2, I-34014 Trieste, Italy*
[16]*Centro de Astrobiología (CAB), CSIC-INTA, Ctra. de Ajalvir km 4, Torrejón de Ardoz, E-28850 Madrid, Spain*

Accepted 2025 February 21. Received 2025 February 15; in original form 2024 May 3

ABSTRACT

We investigate the X-ray properties of a sample of 71 broad- and narrow-line active galactic nucleus (AGN) at $2<z<11$ discovered by *JWST* in the GOODS (Great Observatory Origins Deep Survey) fields, which have the deepest *Chandra* observations ever obtained. Despite the widespread presence of AGN signatures in their rest-optical and -ultraviolet spectra, the vast majority of them is X-ray undetected. The stacked X-ray data of the non-detected sources also results in a non-detection. The upper limit on the X-ray emission for many of these AGN is one or even two orders of magnitude lower than expected from a standard AGN Spectral Energy Distribution (SED). X-ray absorption by clouds with large (Compton-thick) column density and low dust content, such as the broad-line region (BLR) clouds, can explain the X-ray weakness. In this scenario, the BLR covering factor should be much larger than in low-z AGN or luminous quasars; this is supported by the larger equivalent width of the broad component of Hα in *JWST*-selected AGN. We also find that the *JWST*-discovered AGN lack prominent, fast outflows, suggesting that, in *JWST*-selected AGN, dense gas lingers in the nuclear region, resulting in large covering factors. We also note that a large fraction of *JWST*-selected AGN matches the definition of narrow-line Seyfert 1, typically accreting at high rates and characterized by a steep X-ray spectrum – this can further contribute to their observed weakness at high-z. Finally, we discuss that the broad Balmer lines used to identify type 1 AGN cannot be ascribed to very massive stars or supernovae, although we show that some of the faintest broad lines could potentially be associated with superluminous SNe.

Key words: galaxies: high-redshift – galaxies: nuclei – quasars: supermassive black holes – infrared: galaxies – X-rays: galaxies.

1 INTRODUCTION

The launch of the *JWST* is drastically revisiting our understanding of black hole (BH) formation and accretion in the early Universe. Indeed, its unprecedented sensitivity in the infrared (IR) bands has allowed the discovery of several dozens active galactic nuclei (AGNs)

★ E-mail: r.maiolino@mrao.cam.ac.uk

at high redshift ($z \sim 3$–11) with bolometric luminosities ($L_{\rm AGN} \sim 10^{42} - 10^{45}$ erg s^{-1})[1] much lower than probed by previous surveys of high-z quasars.

Most of these AGN have been identified primarily through the detection of a broad component of the permitted emission lines (primarily Hα and Hβ) without a corresponding broad component of forbidden lines (mostly [O III]5007), indicating that it cannot be associated with an outflow and leaving the broad-line region (BLR) around an accreting BH as the most plausible explanation (Furtak et al. 2024; Harikane et al. 2023; Kokorev et al. 2023; Kocevski et al. 2023, 2024; Übler et al. 2023, 2024; Maiolino et al. 2024b, c; Greene et al. 2024; Juodžbalis et al. 2024a).

Additionally, a growing number of narrow-line, type 2 AGN has also been identified by using various diagnostics (Bogdan et al. 2024; Goulding et al. 2023; Perna et al. 2023; Scholtz et al. 2023; Chisholm et al. 2024) and new diagnostic diagrams are being developed to identify type 2 AGN (e.g. Mazzolari et al. 2024).

This new discovery space has revealed important and interesting features of the population of early supermassive BHs. They tend to be overmassive relative to the host galaxy stellar mass, when compared with the local relation (Bogdan et al. 2024; Goulding et al. 2023; Harikane et al. 2023; Maiolino et al. 2024b, c; Übler et al. 2023; Parlanti et al. 2024; Juodžbalis et al. 2024a), indicating that BH formation and growth outpaces star formation in the host galaxy. Some studies have suggested that the observed overmassive nature of these BHs is due to a very large scatter of the $M_{\rm BH} - M_{\rm star}$ relation combined with selection effects (Li et al. 2025). However, high-z BHs are much closer to the local BH–σ relation (Maiolino et al. 2024b; Juodžbalis et al. 2024a) suggesting that the latter relation is more fundamental and universal, and also that selection effects play a secondary role. The BHs discovered by *JWST* have been found to span a broad range of accretion rates, from super-Eddington to orders of magnitude below the Eddington limit. Generally, the results obtained by *JWST* have been interpreted as requiring either massive seeds (e.g. direct collapse BHs) and/or BHs experiencing bursts of super-Eddington accretion (Di Matteo et al. 2023; Pacucci et al. 2023; Schneider et al. 2023; Scoggins, Haiman & Wise 2023; Trinca et al. 2023; Volonteri, Habouzit & Colpi 2023; Zhang et al. 2023; Lupi et al. 2024; Tremmel et al. 2024; Bennett et al. 2024; Natarajan et al. 2024; Rantala, Naab & Lahén 2024; Jeon et al. 2025).

The fraction and density of AGN found by *JWST* depends on the selection criteria and on the depth of the observations. Greene et al. (2024) selected AGN through their red colours; out of a population of red objects accounting for about 1 per cent of the galaxy population, they find that most of them are spectroscopically confirmed as AGN. Matthee et al. (2024) selected AGN from Near Infrared Camera (NIRCam) grism slitless spectra based on the detection of broad Hα; they derive that, about 1 per cent of galaxies in the ultraviolet (UV) luminosity range $-18 < M_{\rm UV} < -20$ host a type 1 AGN with bolometric luminosity higher than $10^{44.5}$ erg s^{-1} at $z \sim 4$–5. Harikane et al. (2023) selected type 1 AGN at lower bolometric luminosities by using Near Infrared Spectrometer (NIRSpec) data finding that the fraction of type 1 AGN at $z \sim 4$–7 ranges from a few per cent to ∼10–15 per cent. Maiolino et al. (2024b) used deep spectroscopic data from the *JWST* Advanced Deep Extragalactic Survey (JADES, Eisenstein et al. 2023) survey to identify AGN at $z > 4$, and found that, in the UV luminosity range $-18 < M_{\rm UV} < -20$, about 10 per cent of galaxies host a type 1 AGN with $L_{\rm AGN} > 10^{44}$ erg s^{-1}. Scholtz et al. (2023) used a smaller sample of the JADES spectra to identify also type 2 AGN, and found that about 20 per cent (in the UV luminosity range $-18 < M_{\rm UV} < -20$) host either a type 2 or a type 1 AGN at $z \sim 5$, down to bolometric luminosities of $\sim 10^{42}$ erg s^{-1}.

These space densities are much higher than the extrapolation of the luminosity function of luminous quasars (Niida et al. 2020), indicating that *JWST* is tracing a different population, which is not surprising. However, even more intriguingly, the population of AGN found by *JWST* is much larger, by about an order of magnitude, than X-ray-selected AGN at similar redshifts (Giallongo et al. 2019). Yet, X-ray-selected AGN resolved about 90 per cent of the X-ray background (XRB) in the 0.5–2 and 2–10 keV bands (Moretti et al. 2003). Therefore, if the AGN discovered by *JWST* share the same spectral energy distribution (SED) as AGN identified locally and at lower redshift, then there is not much scope for an additional large population of AGN within the constraints given by the XRB. This issue was indeed highlighted by Padmanabhan & Loeb (2023), who pointed out that the population of AGN discovered by *JWST* would overproduce the XRB by up to an order of magnitude. However, they assumed an SED inferred from local/low-z AGN and quasars (Shen et al. 2020). Therefore, the main issue is whether this new population of AGN discovered by *JWST* shares the same observed SED as local/low-z AGN and, in particular, the same observed X-ray to optical/UV luminosity ratio. Some studies have already noticed that the *JWST*-identified AGN at high redshift are undetected in the X-rays (e.g. Matthee et al. 2024; Übler et al. 2023). X-ray weakness at high-z was found also in some AGN not selected with *JWST*, such as the red quasars at $z \sim 2$–3 found by Ma et al. (2024) and the red quasar at at $z = 7.2$ discovered by Fujimoto et al. (2022); however, *JWST* is finding a larger AGN population with these properties than previous studies. For instance, more recently, Yue et al. (2024) and Ananna et al. (2024) stacked X-ray data of the so-called little red dots (Greene et al. 2024; Kocevski et al. 2024), many of which are found to host an AGN, and obtained non-detections or marginal detections. However, the little red dots are only a small fraction (∼10 per cent–30 per cent) of the AGN population found by *JWST* (Hainline et al. 2025). A more systemic characterization of the X-ray properties of the bulk of the AGN population discovered by *JWST* at high-z, has yet to be obtained.

Here, we explore the X-ray properties of the AGN discovered by *JWST* in the deepest Chandra fields, the Great Observatory Origins Deep Survey GOODS-N (2 Ms) and GOODS-S (7 Ms) (Alexander et al. 2003; Luo et al. 2017) and demonstrate that they are much fainter in the hard X-rays than expected from the standard SED of AGN, even accounting for its luminosity dependence. We discuss possible scenarios to explain such differences, ranging from heavy obscuration (Compton thick), intrinsic X-ray weakness (associated with high accretion rate and/or lack of a hot corona), and, in a small number of cases, the possible misclassification. We show that there is observational evidence in support of some of these scenarios.

Throughout this work, we use the AB magnitude system and assume a flat Lambda-cold dark matter cosmology with $\Omega_m = 0.315$ and $H_0 = 67.4$ km s^{-1} Mpc^{-1} (Planck Collaboration VI 2020). With this cosmology, 1″ corresponds to a transverse distance of 5.84 proper kpc at $z = 6$.

2 *JWST* SAMPLE OF AGN AND BOLOMETRIC LUMINOSITIES

We focus on AGN discovered (or further characterized) by *JWST* in the GOODS-N and GOODS-S fields. These are the deepest *Chandra* fields and therefore, together with the deep *JWST* spectroscopic data, provide some of the most stringent constraints on the X-ray emission. The primary focus is at $z > 4$, the new AGN frontier explored by

[1]Throughout the paper, $L_{\rm AGN}$ indicates the bolometric luminosity.

JWST at intermediate/low luminosities. However, we consider also some samples at $2<z<4$ to explore whether some of the observed properties are also seen at intermediate redshifts. More specifically, we consider the following samples:

(i) The type 1 AGN at $4 < z < 5.6$ found by Matthee et al. (2024) in GOODS-S and GOODS-N through the detection of a broad component of Hα in the NIRCam grism slitless spectra from the First Reionization Epoch Spectroscopically Complete Observations (FRESCO) survey (Oesch et al. 2023, eight objects in total). In most of these cases, there are no [O III] observations to compare the profile and verify the lack of a broad component. However, the width and strength of the emission lines, together with point-like morphologies, leave little doubt that these are type 1 AGN. Additionally, most of these sources have very red colours in the reddest NIRCam bands, suggesting that they are absorbed with $A_V \sim 1-4$ mag.

(ii) The type 1 AGN discovered with NIRSpec Micro Shutter Array (MSA, Ferruit et al. 2022; Jakobsen et al. 2022; Böker et al. 2023) observations in GOODS-N and GOODS-S at $4< z < 11$ as part of the JADES survey (Eisenstein et al. 2023) from Maiolino et al. (2024b, 13 objects in total). These are selected through the detection of a broad component of Hα (and in one case Hβ), without a corresponding broad component of [O III]5007. The only exception is GN-z11, for which the detection of a type 1 AGN is identified through densities typical of the BLR, via the UV semiforbidden lines of N III] and N IV], and for which the presence of the AGN is also confirmed by other AGN-like transitions (CII* and [Ne IV]), fast outflows revealed in C IV (Maiolino et al. 2024c), ionization cones (Maiolino et al. 2024a). and a large Lyα halo typical of high-z quasars (Scholtz et al. 2024). The X-ray non-detection of GN-z11 was already discussed in Maiolino et al. (2024c), and the upper limits were pointed out to be consistent with the narrow-line Seyfert 1 (NLSy1) nature of GN-z11.

(iii) The type 1 AGN GS_3073 at $z=5.5$ in GOODS-S. This was originally considered to be an AGN by Vanzella et al. (2010) and Grazian et al. (2020) based on the detection of N V and N IV] in the UV rest-frame, with ground-based spectroscopy. It was then found to be a type 1.8 AGN by Übler et al. (2023) based on the detection of broad components of multiple permitted lines (H, He I, and He II) in NIRSpec Integral Field Spectroscopy (IFS, Böker et al. 2022) data. Übler et al. (2023) and Ji et al. (2024) detected also several additional high ionization transitions, including coronal lines. The lack of X-ray detection of this AGN was already mentioned in the papers above, but will be quantified more in detail in this paper.

(iv) The dormant BH at $z=6.7$ found by Juodžbalis et al. (2024a) in JADES, through the detection of a broad component of Hα.

(v) We also include XID403, an X-ray-selected, Compton-thick AGN at $z=4.76$ in GOODS-S initially discovered by Gilli et al. (2011). This galaxy has been recently observed with NIRSpec–IFS revealing a clear broad component of the Hα line, indicating that this is actually a reddened type 1 AGN, whose X-rays are heavily absorbed by a Compton-thick medium (Parlanti et al. 2024).

(vi) We include six additional type 1 AGN at $2<z<4$ found in the public DR3 of JADES (D'Eugenio et al. 2025). One of these is characterized by deep, slightly blueshifted absorption of Hα, Hβ, and He I (Juodžbalis et al. 2024b).

(vii) We also consider the sample of 41 type 2, narrow-line AGN found by Scholtz et al. (2023) at $2<z<9$ based on NIRSpec–MSA spectra from JADES. As the classical type 2 classification based on the Baldwin-Phillips-Terlevich (BPT) diagrams breaks down at high redshift for intermediate-luminosity and low-metallicity AGN (Kocevski et al. 2023; Maiolino et al. 2024b; Übler et al. 2023), Scholtz et al. (2023) identified type 2 AGN also based on the detection of high ionization transitions and diagnostic diagrams based on UV transitions. The sample of Scholtz et al. (2023) also includes GS-21150, which was allocated a slit in the JADES MSA Deep survey, because X-ray detected; this galaxy was identified spectroscopically to have a redshift of 3.08, however none of the optical or UV diagnostics indicate that it hosts an AGN.

(viii) Finally, we include the type 2 AGN at $z = 5.6$ found by Chisholm et al. (2024) via the detection of [Ne V] with NIRSpec–MSA.

Overall, type 1 AGN are primarily identified through the identification of a broad component of Hα (and in some cases of Hβ and other permitted lines). However, the sensitivity in detecting broad lines is different in the various surveys, with the slitless grism surveys being the least sensitive, while the JADES slit survey being the deepest. Additionally, the parent samples are heterogeneous: the slitless surveys provide an unbiased sample of broad-line AGN down to their sensitivity limit; multislit (MSA) spectroscopy has, for different surveys, a complex selection function, primarily based on multiband photometric redshifts and a limiting magnitude to ensure continuum or (narrow) lines detection, but generally without a priori knowledge for the presence of an AGN.

The type 2 AGN sample is selected with a variety of narrow-line diagnostics, primarily consisting of the detection of high ionization lines and UV/optical diagnostics diagrams calibrated with models or empirically. The parent sample of the large type 2 sample from Scholtz et al. (2023) has the same heterogeneity as discussed above.

Despite the heterogeneous diagnostics of the parent samples, all these AGN have in common the fact that they probe a low-/intermediate-luminosity regime at high redshift, not probed by previous samples, and that were not pre-selected because known to have an AGN from previous observations (with the exception of the two X-ray-selected objects discussed above). Additionally, these *JWST*-idenfied AGNs are typically hosted in low-mass ($M_* \sim 10^8$–10^{10} M$_\odot$) and metal-poor ($Z \sim 0.1$ Z$_\odot$) host galaxies, in contrast with more luminous quasars at similar redshifts.

The bolometric luminosities of type 1 AGN were not inferred from the continuum (with the exception of GN-z11, see Maiolino et al. 2024c) as it may be dominated by the host galaxy or by reflected light. They are instead homogeneously estimated from the extinction-corrected broad component of Hα and adopting the scaling relation provided by Stern & Laor (2012). For type 2 AGN, the bolometric luminosity is inferred from the extinction-corrected [O III]5007 line and adopting the scaling relation given in Scholtz et al. (2023), based on the photoionization models obtained by Hirschmann et al. (in preparation). We will however also illustrate the effect of using the scaling relations provided by Netzer (2019), which typically give luminosities that are 0.5 dex higher.

The full sample of AGN, with their primary properties, is given in Tables 1 and 2, for type 1 and type 2 respectively.

3 X-RAY DATA

All the sources discussed in this paper are in either the Chandra Deep Field North (hereafter CDF-N) or the Chandra Deep Field South (hereafter CDF-S). CDF-N and CDF-S are the two deepest X-ray surveys to date, with a total exposure of 2 and 7 Ms, respectively, and an on-axis flux limit in the 0.5–2.0 keV band of 2.5×10^{-17} erg cm^{-2} s^{-1} (CDF-N, Alexander et al. 2003) and 6.4×10^{-18} erg cm^{-2} s^{-1} (CDF-S, Luo et al. 2017). This on-axis sensitivity significantly decreases for sources in the outer regions of the fields (see Alexander et al. 2003; Luo et al. 2017, for details).

Table 1. Sample properties and results of the X-ray spectral analysis for the type-1 sources. The first group of 21 lines describes the JADES and GA-NIFS sources at redshift $z > 4$. In the following three lines we report the values for the stacked spectra relative to the whole sample and the low- and high-luminosity subsamples. We also include the data for six AGNs in the same fields with redshift $2 < z < 4$, and for two relevant additional sources: XID 403 (Gilli et al. 2011, see the text for details) and GN 1 146 115 (Juodžbalis et al. 2024a). All upper limits are estimated at a 90 per cent significance level.

ID	z	$\log(M_{BH})$	$\log(L_{BOL})$	$\log(L/L_{Edd})$	F(2–10 keV)	L(2–10 keV)	L_{BOL}/L_X
GS 10 013 704	5.919	7.5	44.32	−1.26	<1.40E−17	<3.08E + 42	>68
GS 8083	4.647	7.3	44.53	−0.80	<5.15E−18	<6.88E + 41	>498
GN 1093	5.594	7.4	44.75	−0.69	<7.33E−17	<1.44E + 43	>39
GN 3608	5.269	6.8	43.95	−0.95	<7.33E−17	<1.28E + 43	>7.1
GN 11 836	4.409	7.1	44.51	−0.70	<8.97E−18	<1.07E + 42	>308
GN 20 621	4.682	7.3	44.64	−0.74	<3.07E−17	<4.17E + 42	>105
GN 73 488	4.133	7.7	44.98	−0.80	<8.53E−17	<8.88E + 42	>110
GN 77 652	5.229	6.9	44.52	−0.43	< 2.02E−17	<3.48E + 42	>95
GN 61 888	5.874	7.2	44.80	−0.50	<3.52E−17	<7.60E + 42	>84
GN 62 309	5.151	6.6	44.23	−0.41	<4.01E−17	<6.67E + 42	>26
GN 53 757	4.447	7.7	44.42	−1.35	<6.53E−17	<7.96E + 42	>34
GN 954	6.759	7.9	45.60	−0.38	<3.62E−17	<9.80E + 42	>409
GS 3073	5.55	8.2	45.68	−1.13	< 1.64E−17	<3.19E + 42	>1514
GN 4014	5.228	7.58	44.95	−0.71	<5.84E−17	<1.00E + 43	>89
GN 9771	5.538	8.55	45.80	−0.83	<3.75E−17	<7.26E + 42	>873
GN 12 839	5.241	8.01	45.47	−0.62	<1.78E−17	<3.07E + 42	>978
GN 13 733	5.236	7.49	44.70	−0.87	<2.60E−17	<4.47E + 42	>112
GN 14 409	5.139	7.21	44.85	−0.44	< 2.11E−17	<3.49E + 42	>204
GN 15 498	5.086	7.71	45.00	−0.79	<4.30E−17	<6.96E + 42	>144
GN 16 813	5.355	7.55	44.94	−0.69	<5.58E−17	<1.00E + 43	>87
GS 13 971	5.481	7.49	44.72	−0.85	<2.08E−17	<3.95E + 42	>134
GN-z11	10.604	6.2	44.98	0.7	<1.60E−17	<8.85E + 42	>109
ALL	5.237	–	45.05	–	<3.74E−18	< 3.17E + 41	> 3571
ALL-Low-L	5.097	–	44.53	–	<3.43E−18	< 6.87E + 41	> 497
ALL-High-L	5.390	–	45.29	–	<4.07E−18	< 4.34E + 41	> 4527
GN 28 074	2.259	8.27	48.21	−0.75	<1.1E−17	<2.8E + 41	>15402
GN 721	2.942	7.95	45.80	−1.21	1.1±0.4E−16	4.7E + 42	151
GS 49 729	3.189	8.46	42.96	−1.48	2.1±0.3E−15	9.5E + 43	13
GS 17 341	3.598	6.52	46.55	−0.58	<1.4E−17	<9.6E + 41	>117
GN 2916	3.664	6.77	45.96	−1.02	<4.6E−17	<3.4E + 42	>22
GS 209 777	3.711	8.90	45.40	−1.59	1.5±0.1E−15	1.3E + 44	15
GS 13 329	3.936	6.75	45.28	−0.72	<2.0E−17	<1.6e42	>85
XID 403	4.76	–	45.28	–	6.6E−16	6.5E + 42	> 293
GN 1 146 115	6.68	8.6	45.11	−1.62	<1.5E−17	<3.9E + 42	> 329

The total exposure in both fields has been achieved through many individual observations (102 for the CDF-S and 20 for the CDF-N). Since each source is located in different positions during each individual observations, calibrations and point spread function (PSF) change for each observation. Therefore, in order to obtain accurate spectral information (in particular, to correctly estimate flux upper limits) we extracted and calibrated the X-ray spectral counts (source + background) from each individual *Chandra* exposure. This was done by using the CIAO 4.16 package (Fruscione et al. 2006), and regardless of the presence (or absence) of a detected source. Since in almost all cases the source is not detected, this amounts to extracting a background spectrum. The optimal radius of the circular extraction region depends on the source position (due to the highly variable PSF across the field of view of *Chandra*), and has been chosen in order to include 90 per cent of the effective area at that position. The 'true' background has been extracted from an annular region with the same centre, paying attention to remove any serendipitous source present in the chosen annulus. Calibrations were computed for individual exposures too. The individual spectral data and calibrations have then been stacked to produce a total source and background spectrum.

The evaluation of the flux upper limits has been performed through a spectral analysis[2] with the XSPEC 12.6 package (Arnaud 1996). We assumed a power-law model with a fixed photon index $\Gamma = 1.7$ and a Galactic absorption. The photon index Γ=1.7 has been chosen in order to test the scenario of 'standard' AGN, which are typically characterized by this X-ray spectral slope. Having fixed the photon index and Galactic absorption, the only free parameter was the source flux. In order to derive such flux, we formally fitted the data in the 0.5–5 keV (observed frame) interval, corresponding to a rest-frame energy range of 2.5–25 keV at $z = 4$. We considered the source as detected if the flux best-fitting value is higher than zero with a statistical significance of at least 3σ. In case of non-detections, we computed the 90 per cent upper limit with respect to the best-fitting value. The entire procedure was carried out on grouped spectra,

[2]With 'spectral analysis' here we mean a procedure that follows for our non-detections the same steps as a standard spectral analysis, formally treating the counts (source + background) at the source positions as spectra. The upper limits are obtained from the error estimate of the flux for this (background-subtracted) component.

Table 2. Sample properties and results of the X-ray spectral analysis of the sample of type 2 AGNs.

ID	z	$\log(L_{\rm BOL})$	F(2–10 keV)	L(2–10 keV)	$L_{\rm BOL}/L_X$
GS 143 403	0.734	41.26	< 3.5E−18	< 7.2E39	>25.7
GS 10 040 620	1.776	41.63	< 5.6E−18	< 1.3E41	>3.4
GS 10 012 005	1.862	41.44	< 5.9E−18	< 1.5E41	>1.9
GS 8456	1.884	41.56	< 1.5E−17	< 2.9E42	>0.1
GS 209 979	1.896	42.68	< 3.1E−17	< 2.4E42	>2.0
GS 10 036 017	2.015	44.08	< 1.9E−17	< 5.8E41	>216.5
GS 10 012 511	2.019	41.66	< 7.2E−18	< 2.2E41	>2.2
GS 10 008 071	2.227	43.12	< 1.6E−17	< 6.1E41	>21.7
GS 8880	2.327	41.95	< 6.3E−18	< 2.7E41	>3.3
GS 17 670	2.349	42.99	< 5.9E−18	< 2.6E41	>38.2
GS 10 073	2.631	42.98	< 1.0E−17	< 5.7E41	>16.9
GS 10 011 849	2.686	43.58	< 5.4E−18	< 3.3E41	>119.7
GS 7099	2.860	42.87	< 5.8E−18	< 4.1E41	>18.5
GS 114 573	2.880	42.28	< 1.0E−17	< 4.8E41	>4.1
GS 111 511	3.002	42.50	< 1.4E−17	< 7.4E41	>4.4
GS 132 213	3.017	42.17	< 5.0E−18	< 2.6E41	>5.7
GS 10 013 597	3.319	42.60	< 3.6E−17	< 3.7E42	>1.1
GS 10 035 295	3.588	43.70	< 1.4E−17	< 1.8E42	>29.1
GS 104 075	3.719	43.14	< 8.0E−18	< 6.6E41	>21.3
GS 108 487	3.974	41.91	< 3.8E−17	< 3.7E42	>0.2
GS 7762	4.145	43.62	< 2.2E−17	< 3.8E42	>11.1
GS 95 256	4.162	42.08	< 1.0E−17	< 1.1E42	>1.1
GS 8073	4.392	44.38	< 1.1E−17	< 2.2E42	>130.1
GS 10 000 626	4.467	42.51	< 1.6E−17	< 3.2E42	>1.0
GS 111 091	4.496	42.03	< 2.3E−17	< 2.9E42	>0.4
GS 17 072	4.707	42.29	< 1.4E−17	< 3.3E42	>0.6
GS 10 015 338	5.072	43.85	< 4.5E−18	< 1.3E42	>57.5
GS 9452	5.135	43.59	< 1.2E−17	< 3.4E42	>11.8
GS 202 208	5.453	44.88	< 3.2E−17	< 6.0E42	>140.5
GS 208 643	5.566	43.61	< 1.1E−17	< 2.2E42	>18.5
GS 16 745	5.573	43.71	< 1.6E−17	< 3.5E42	>14.9
GS 22 251	5.804	44.08	< 8.0E−18	< 3.0E42	>40.2
GS 10 056 849	5.820	43.16	< 1.9E−17	< 7.1E42	>2.1
GS 201 127	5.837	43.45	< 3.0E−17	< 6.5E42	>4.4
GS 99 671	5.936	43.17	< 1.8E−17	< 4.0E42	>3.8
GS 9422	5.942	44.47	< 9.3E−18	< 3.7E42	>81.9
GS 10 013 609	6.930	43.94	< 9.2E−18	< 5.3E42	>16.5
GS 10 013 905	7.206	43.67	< 5.8E−18	< 3.7E42	>12.9
GS 21 842	7.981	43.76	< 4.9E−18	< 3.9E42	>15.1
GS 10 058 975	9.436	44.36	< 8.9E−18	< 2.9E43	>8.1
STACK1	($z<3$, @$z=2$)	42.53	< 6.3E−19	< 1.3E40	> 273
STACK2	($z>3$, @$z=5$)	43.58	< 1.4E−19	< 2.0E40	> 990
GN 42 437	5.59	44.38	< 7.4E−17	<1.4E43	>17.9
GS 21 150	3.8	43.78	1.6E−16	2.0E42	31.5

Notes. [a]Flux and luminosity obtained from a fit with a power law with slope $\Gamma = 1.7$. All upper limits are estimated at a 90 per cent significance level.

ensuring at least one count per bin, and analysed using W-statistics – a modified version of C-statistics in which the background spectrum is subtracted rather than fitted independently. This approach is well suited to our case, given the relatively high background level resulting from the long exposures of the CDF observations, which ensures at least one background count per bin for almost all sources.

Fluxes and upper limits have been estimated in the 2–10 keV energy range both in the observed and the rest frames (in this case we used an extension of the instrumental response to energies slightly lower than 0.5 keV when needed).

These values are reported in Tables 1 and 2 for type 1 and type 2 objects, respectively. We have checked that overall our estimates are consistent with the *Chandra* upper-limit maps of Xue et al. (2016) and Luo et al. 2017.

We note that while for most of the sources the net counts after background subtraction are consistent with zero within 1σ, in a few cases they are above zero with a statistical significance between 1σ and 2σ. We treat these cases as non-detections, considering that our upper limits estimate automatically take into account the level of these possible marginal detections. Indeed, the two sources with a signal-to-noise ratio (S/N) above zero at the $\sim 1.5\sigma$–2σ level, GN 3608 and GN 73488, have the two highest flux upper limits in our sample (Table 1).

The images shown throughout the paper have been extracted from the merged images of both fields and are intended for visual inspection only.

As is clear from Tables 1 and 2, the vast majority of the *JWST*-identified AGN are undetected with *Chandra*. Out of the five detected

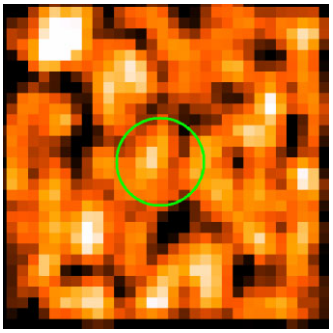

Figure 1. *Chandra* X-ray image of the type 1.8 AGN GS_3073, which is one the most luminous $z > 4$ targets in our sample, thoroughly studied (Übler et al. 2023; Ji et al. 2024), and whose AGN nature is unambiguously confirmed by numerous rest-optical and rest-UV diagnostics. The image does not reveal a detection, while a $\sim 20\sigma$ detection would have been expected based on a standard AGN SED. The radius of the circular region is 3 arcsec.

sources, two had been originally selected in the X-rays, and will be discussed in the next sections. The remaining three objects, GN 721, GS 49 729, and GS 209777, are type 1 AGN at redshift $z \sim 3$ (Table 1). GN 721 is detected with a statistical significance of $\sim 5\,\sigma$, so only a basic spectral analysis is possible. We repeated the spectral analysis for these objects allowing for a free photon index, finding a low value ($\Gamma = 0.1 \pm 0.6$) suggesting a Compton-reflection spectrum. The bolometric to X-ray ratio for this source is $\sim$10 times higher than in typical optically selected AGN (see discussion in the next section). This is of the same order as the ratio between the flux of the primary X-ray power law and the Compton-reflection component in local AGN in the same rest-frame interval (1.5–15 keV). Therefore, the X-ray weakness of GN 721 could be interpreted as due to absorption and reflection by a 'standard' Compton-thick circumnuclear torus of an otherwise typical intrinsic X-ray emission. The remaining two sources, GS 49 729 and GS 209777, have high S/N detections in the CDF-S field, and show X-ray properties typical of a 'normal' AGN: their spectra are well reproduced by an unobsorbed power law with a photon index $\Gamma = 1.65 \pm 0.05$ and 1.7 ± 0.1, respectively, and their bolometric to X-ray flux ratios are typical of optically selected AGN (see the next section).

Considering that the low photon index found in GN 721 may be common among our sources, we repeated the upper limits estimates assuming a value $\Gamma = 0$ for the whole sample. While the individual flux upper limits may change within a factor of two, the overall distribution does not significantly change. Therefore, in the remainder of the paper we will always refer to the upper limits obtained assuming $\Gamma = 1.7$.

In order to increase the sensitivity of our analysis, we also produced stacks in luminosity bins, which also give non-detections, and yield upper limits down to a few times 10^{-18} erg s^{-1} cm^{-2} and a few times 10^{-19} erg s^{-1} cm^{-2}, for the type 1 and type 2 samples, respectively. Note that the upper limit on the type 2 sample is more stringent both because there are more type 2 AGN and because the analysis performed by Scholtz et al. (2023), out of which our type 2 sample is extracted, is done only in GOODS-S, where the *Chandra* observation is deeper.

We do not show the images and spectra for all non-detections. We only show, as an example, the image for the remarkable case of the type 1.8 AGN GS_3073. As we will discuss further later on, this is a fairly luminous AGN with multiple unambiguous UV and optical AGN signatures. As illustrated in Fig. 1, despite being in the deepest region of the CDFS 7 Ms area, it is not detected.

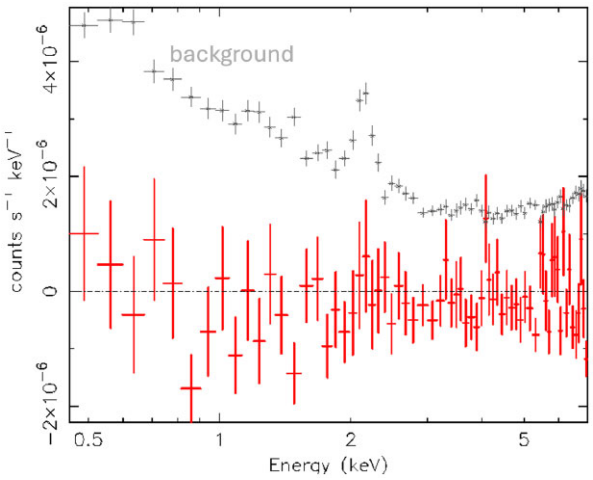

Figure 2. Stacked X-ray spectrum for the whole sample of *JWST*-identified type 1 AGN. The upper grey spectrum shows the background level.

Fig. 2 shows the X-ray spectrum obtained for the stack of all type 1 AGN found by *JWST* in the GOODS fields, which shows no detection. We have also stacked this sample after splitting it in two bins of high and low luminosities, with a dividing value of $\log(L_{\rm BOL}) = 44.8$ (in units of erg s^{-1}), consisting of 11 and 12 sources, respectively. These stacks are shown in Appendix A, and do not show any detection either. The thumbnails associated with these stacks are shown in Fig. 3. The stacking of type 2 AGN is shown in Fig. 4, also in this case not showing any detection.

4 EXTREMELY HIGH $L_{\rm Bol}/L_X$

The previous section has shown that the vast majority of AGN identified by *JWST*, both type 1 and type 2, are not detected even with the deepest *Chandra* observations, not even in stacking. A similar result was obtained, at lower redshifts, by Lyu et al. (2024) when exploring the X-ray counterparts of AGN photometrically identified in the mid-IR.

The only X-ray-detected AGN at $z > 4$ in our sample is XID403. This is primarily because it was initially selected based on its X-ray emission and subsequently observed with *JWST*. In the type 1 AGN sample at $z < 4$ there are two X-ray detections out of six objects. There is only one type 2 AGN in the sample by Scholtz et al. (2023) that is X-ray detected, at $z = 3.08$; however, we note that this source was allocated a slit in the JADES survey because previously known to be X-ray detected, but its *JWST* spectrum does not reveal any AGN signature.

As far as we know, there is currently only one other high-z AGN spectroscopically identified by *JWST* that is detected in the X-rays, UHZ-1 at $z = 10.1$, identified by Bogdan et al. (2024) and Goulding et al. (2023). As XID403, UHZ-1 is a candidate Compton-thick source, based on its X-ray spectrum. Its *JWST* spectrum does not reveal any AGN signature, further revealing the frequent disconnect between X-ray and optical/UV AGN diagnostics.

In this section, we investigate whether these non-detections, even in stacking, are inconsistent with standard AGN SED or if they are merely a result of the sensitivity limits of our observations, instead.

The key aspect to assess is whether the X-ray emission expected from the AGN bolometric luminosity is consistent with the X-ray upper limits or not. It is well known that AGN become X-ray weaker at high (quasar-like) bolometric luminosities (e.g. Duras

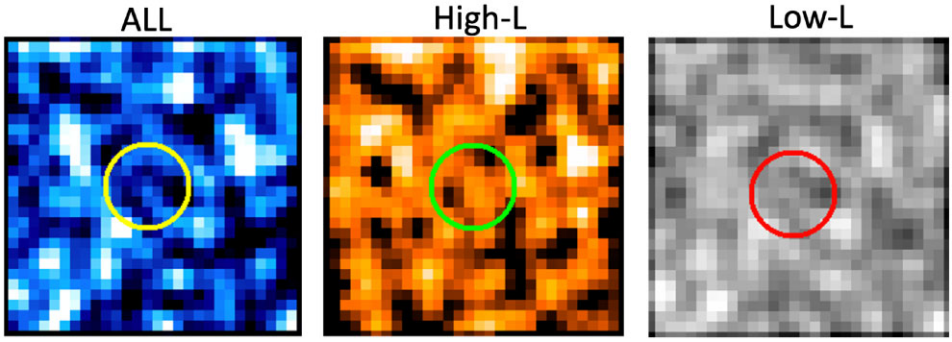

Figure 3. Stacked *Chandra* X-ray images of the whole type 1 AGN sample (left panel) and for the high- and low-luminosity subsamples (middle and right panels, respectively). The radius of the circular region is 3 arcsec. The individual images are from different positions in the CDF-N and CDF-S fields, so they are shown for illustrative purposes only. All the fluxes have been derived from a spectral analysis of each individual source, as described in the text.

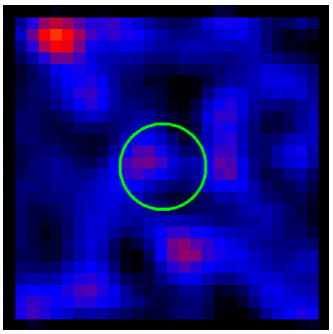

Figure 4. Stacked *Chandra* X-ray images of the whole type 2 AGN sample. The radius of the circular region is 3 arcsec.

et al. 2020; Shen et al. 2020). Hence, it is important to compare the *JWST*-detected AGN with the SED inferred for low-z/local AGN with the same bolometric luminosity. Fig. 5 shows the distribution of optically/UV-selected type 1 AGN at $z < 0.6$ from Lusso et al. (2020) (light blue small symbols) on a diagram where bolometric to hard X-ray luminosity ratio ($k_{\rm bol,X} = L_{\rm bol}/L_{[2-10\ {\rm keV}]}$) is plotted as a function of bolometric luminosity. The black line shows the best-fitting relation for local/low-z quasars and AGN identified by Duras et al. (2020). We note that luminous (optically/UV selected) quasars at $z > 6$ follow the same relation as the local/low-z AGN (Zappacosta et al. 2023), or possibly slightly above the relation in terms of $k_{\rm bol,X}$ (Vito et al. 2019).

The large solid symbols indicate the values (mostly lower limits) inferred for the type 1 AGN identified by *JWST* in our GOODS-N/S sample.

The only detection in the $z > 4$ sample is the Compton-thick AGN XID403, indicated by the upper blue diamond, while the lower diamond (connected with a dashed segment) indicates the X-ray absorption corrected value. It illustrates that the observed $L_{\rm Bol}/L_{\rm X}$ is well above the local, standard relation, while the corrected value is perfectly consistent with the relation. All other $z > 4$ objects are lower limits, most of which are highly significant, i.e. well above the relation and its dispersion. Particularly luminous AGN which lacked X-ray detection, and which were individually discussed in the previous section, are marked with specific symbols (see the legend) and are also well above the local relation. Remarkable is GS_3073, which, as we mentioned, is an extremely well studied AGN at $z = 5.55$ with multiple unambiguous AGN signatures, located in the deepest region of the *Chandra* 7 Ms pointing and, despite this, undetected and more than one order of magnitude above the standard relation.

The stacked X-ray limit for the $z > 4$ type 1 sample is shown with a starred red symbol, for the total sample (we do not plot the two stacks in two luminosity for the sake of clarity of an already overcrowded plot, but they convey the same information as the total stack, i.e. very high $L_{\rm bol}/L_{\rm X}$). These stacks provide some of the tightest constraints on the bolometric to X-ray ratio, deviating by more than two orders of magnitude relative to the local relation.

The black squares show the measurements for the (smaller) type 1 sample at $2 < z < 4$. Most of them are upper limits, and most of these well above the local relation. In this case, as discussed in the previous section, there are three detections: GN 721 is well above the local relation, and is characterized by an X-ray spectrum suggestive of Compton thickness; GS 49 729 and GS 209 777 are consistent with the local relation, and their X-ray spectrum is consistent with a typical type 1 AGN without absorption.

Fig. 6 shows the same diagram for the type 2 AGN in Scholtz et al. (2023). The black diamond shows the only X-ray-detected galaxy (GS 21150, which was actually included in the sample because X-ray selected, but without AGN spectral signatures). All other type 2 AGN have lower limits on $L_{\rm bol}/L_{\rm X}$. Most of these individual lower limits are less constraining relative to the type 1 AGN. However, the stacked values (starred symbols) are above the local relation by one or two orders of magnitude, for the low-z (blue) and high-z (magenta) bins, respectively. We also indicate with an arrow the effect of using the narrow Hβ to bolometric correction provided by Netzer (2019), which would make the deviations even stronger.

Summarizing, the X-ray analysis of the new population of high-z AGN identified by *JWST*, which have low/intermediate luminosities, reveals that they are significantly underluminous in X-rays compared to the lower redshift AGN population, or to the high-z population of luminous quasars. Specifically, for most of them, the X-ray emission is weaker by one or two orders of magnitude than expected based on their bolometric luminosity and assuming a local/standard AGN SED.

5 SCENARIOS

We now discuss the possible scenarios that could explain the X-ray weakness of the *JWST*-discovered AGN. There are three main scenarios: heavy absorption in the X-rays; intrinsic X-ray weakness; and misidentification of AGN. We anticipate that the latter case is very unlikely to play a significant role, as the same X-ray weakness is found independently of the AGN selection and identification

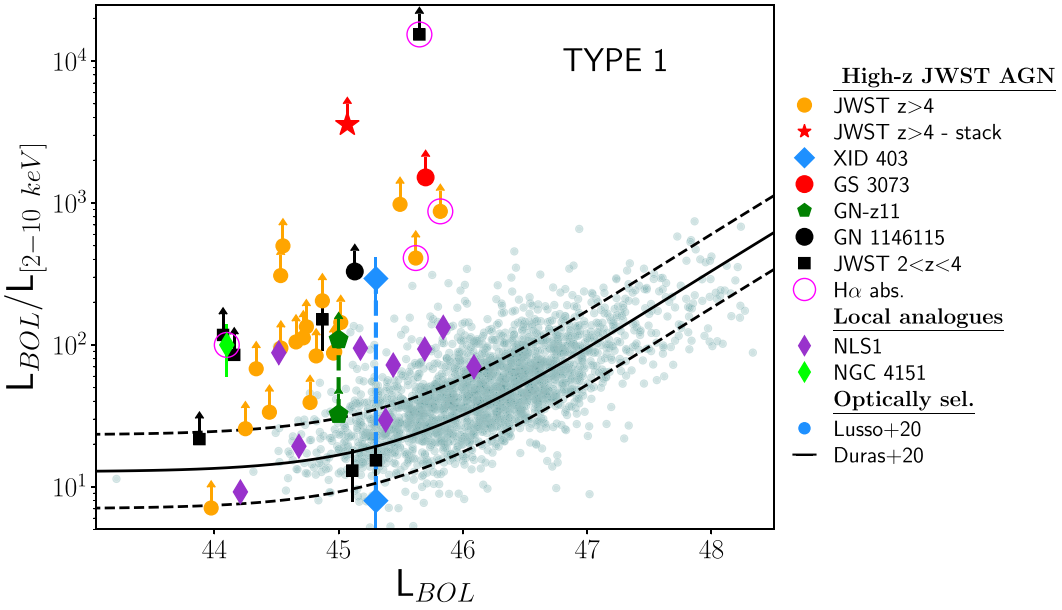

Figure 5. Ratio $k_{\rm bol,X}$ between the AGN bolometric luminosity and the X-ray (2–10 keV) luminosity as a function of the bolometric luminosity $L_{\rm BOL}$ for our sample of type 1 AGN. Light blue small points are from the low-redshift sample of Lusso et al. (2020), and are representative of 'normal', optically/UV-selected blue quasars. The light black lines show the best fit (continuous line) and dispersion (dashed lines) of the $k_{\rm bol,X}$–$L_{\rm BOL}$ relation for quasars from Duras et al. (2020). Purple diamonds show local NLSy1, while the light green diamond shows the prototypical broad-line Seyfert 1 NGC 4151. Orange solid circles show all lower limits in $k_{\rm bol,X}$ for our sample of type 1 AGN at $z > 4$. The star shows the lower limit for the stacked spectra from the whole sample at $z > 4$. We also identify a few relevant sources, as shown in the figure legend (see the text). The black squares show a group of lower redshift ($2<z<4$) type 1 AGN in JADES, two of which are detected. Sources with indication of absorption features in their broad Hα profile are highlighted with magenta empty circles. The bottom and top points relative to the source XID 403 refer to the observed and intrinsic X-ray luminosity, respectively. The bottom and top points relative to GN-z11 indicate two different ways of estimating its X-ray upper limit (see the text).

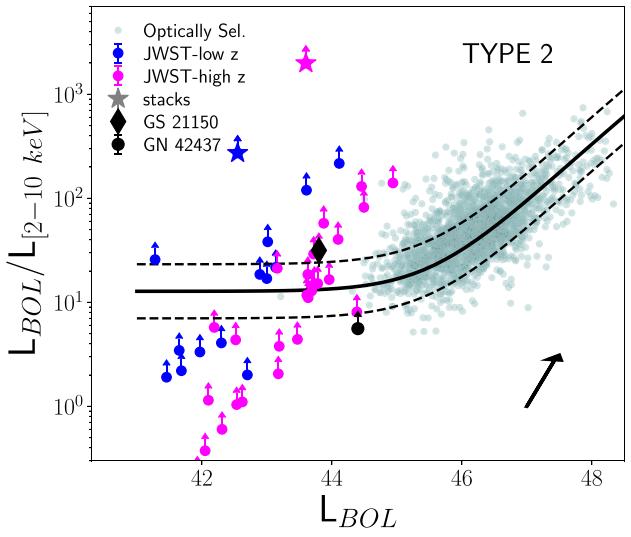

Figure 6. Same as Fig. 5, but for the type 2 sample. Blue and magenta points represent sources at redshift $z < 3$ and $z > 3$, respectively. Stars show the values for the stacked spectra obtained from the two subsamples. The two sources GS 21150 (the only X-ray-detected object in our sample) and GN 42437 (the only type 2 not in the JADES sample) and are shown with different symbols. The arrow on the bottom-right corner of the plot shows the shift of the positions of the points if the bolometric luminosities are estimated as described in Netzer (2019, using their relation between narrow-Hβ and bolometric luminosity) instead of as in Scholtz et al. (2023).

method (broad lines, narrow-line diagnostics, and mid-IR excess). Additionally, there are several cases, such as GS_3073, which are AGN beyond any doubt [strong broad permitted H and He lines, high ionization lines with high equivalent width (EW), and even coronal lines], which are extremely X-ray weak. However, we will discuss that some contamination for a minority of cases is potentially possible.

Most probably, a combination of all the effects discussed above is responsible for the X-ray weakness. However, we will focus primarily on the heavy obscuration scenario, as there is observational evidence that this is likely the case for a significant fraction of the sources.

Independently of the origin of the X-ray weakness, our finding that the bulk of the *JWST*-discovered AGN are extremely X-ray weak, i.e. they do not share the same SED as classical AGN templates, explains why their high abundance does not violate the XRB.

5.1 Compton-thick, high covering, dust-poor absorption

At the redshifts probed by the many AGN in our sample ($z \sim 4$–7), the most sensitive *Chandra* energy range (0.5–2 keV) probes the 4–14 keV rest-frame range, and even higher energies for the most distant AGN in our sample. If the lack of detections is due to X-ray absorption, then this would imply Compton thickness, i.e. $N_{\rm H} > 10^{24}$ cm^{-2}. If the column density is high enough to totally absorb the direct X-ray spectrum, then the observed X-ray spectrum depends on the amount of cold and warm scattered emission. The latter depends strongly on the covering factor and on the column density of the reflecting medium (and on whether the reflected light is

absorbed too) which, in the 2–10 keV band, can go from a few per cent of the direct radiation, to potentially zero.

In the local Universe, the fraction of obscured AGN is about 80 per cent and, of these, the fraction of Compton-thick AGN is estimated to be of the order of 50 per cent (Maiolino et al. 1998; Bassani et al. 1999; Risaliti, Maiolino & Salvati 1999; Risaliti, Elvis & Nicastro 2002; Ananna et al. 2019). There have been studies suggesting an increase of the obscured fraction at high redshift, and also an increasing fraction of Compton-thick AGN, especially in the low-luminosity regime (Buchner et al. 2015; Ananna et al. 2019; Gilli et al. 2022; Peca et al. 2023; Signorini et al. 2023).

The potential issue with the *JWST* findings is that, in order to entirely explain the X-ray weakness with the Compton-thick scenario:

(i) most of the newly discovered AGN should be Compton thick, i.e. the Compton-thick material should be covering nearly 4π the AGN;
(ii) given that obscuration affects most type 1 AGN too, the Compton-thick material should be dust-poor, or even dust-free.

To give a more quantitative assessment of the latter issue, for a standard gas-to-dust ratio and Galactic extinction curve, a Compton-thick medium ($N_{\rm H} > 10^{24}$ cm^{-2}) should give $A_V > 500$ (Maiolino et al. 2001a). Even taking into consideration that at high redshift these galaxies are characterized by metallicities of the order of 0.1 solar, and that the dust-to-metal ratio is lower by a factor of about ~ 2 at such low metallicities (D'Eugenio et al. 2024; Tacchella et al. 2024), Compton-thick absorption should still result in $A_V > 25$. Although some dust reddening is typically seen in most high-z type 1 AGN found by *JWST*, these are in the range of $A_V \sim 0.5 - 4$ (Harikane et al. 2023; Matthee et al. 2024; Maiolino et al. 2024b; Übler et al. 2023; Juodžbalis et al. 2024a), and anyway $A_V > 25$ would certainly totally absorb the broad lines.

A major mismatch between X-ray absorbing column density and dust extinction in AGN, up to a factor of 100 relative to what is expected from the Galactic dust-to-gas ratio, has been known for a long time (Maiolino et al. 2001a). Although peculiar dust properties in the dense nuclear region of AGN may be partially responsible for this effect (Maiolino, Marconi & Oliva 2001b; Gaskell et al. 2004), extensive X-ray variability studies have clearly demonstrated that the bulk of the X-ray absorption, especially at high column densities, happens within the dust sublimation radius, on scales typical of the BLR (Risaliti et al. 2002, 2005, 2011; Maiolino et al. 2010; Nardini & Risaliti 2011). More precisely, when probed with high enough temporal resolution, and with high enough S/N, the observed X-ray absorption is seen to be highly variable, and even changing from Compton thick to Compton thin, consistent with being associated with clouds of the BLR transiting along the line of sight. The BLR is inside the sublimation radius, hence dust-free. On the other hand, both the X-ray variability studies, and photoionization modelling, indicate that the BLR clouds have large columns of gas, generally in excess of 10^{24} cm^{-2}. Therefore, absorption by the BLR clouds along our line of sight can very naturally explain extremely high values of N_H/A_V, and this may be the case also for the AGN newly discovered at high redshift by *JWST*. The latter do actually show some degree of reddening, so it is possible that some of the absorption is also associated with gas outside the BLR and in the host galaxy.

In summary, absorption by BLR clouds, and possibly additional absorption in the host galaxy, can account for extremely Compton-thick X-ray obscuration with modest (or no) dust extinction in the optical/UV. However, the issue with the *JWST*-discovered AGN at high-z is that, if this is the explanation for their X-ray weakness, given the large number of AGN without X-ray detection, the covering factor of the BLR clouds should be close to unity. This would be a quite different BLR distribution relative to the local AGN or high-luminosity quasars at high-z, as in these cases the BLR covering factor is estimated to be of the order of 10 per cent–20 per cent (Netzer 1990; Peterson 2006), although some recent works model the BLR with a covering of up to 50 per cent (Ferland et al. 2020; Guo et al. 2020), possibly as a function of the accretion rate (this aspect will be discussed later in this section). Additionally, the BLR in local and high-luminosity AGN is found to be primarily distributed in a disc-like configuration, probably coplanar with the obscuring torus (or disc of the host galaxy), hence making it much more unlikely for the line of sight to cross a BLR cloud without being totally obscured also by dust in the torus (Mannucci, Salvati & Stanga 1992; Elvis 2000; Maiolino et al. 2001d; Gravity Collaboration 2018; Pancoast et al. 2018).

Therefore, a possible scenario is that, unlike local AGN and high-luminosity quasars, in the high-z AGN newly discovered by *JWST* the ($\sim$ dust-free and Compton thick) BLR clouds are distributed more isotropically around the accretion disc and with a much larger covering factor, possibly approaching unity. Fig. 7 schematically illustrates this scenario and in the following subsection we further investigate its plausibility.

Finally, we shall mention that according to King (2025), a highly Compton-thick envelope of the accreting BH is expected in a scenario of super-Eddington accretion. This will be discussed further in Section 5.2.1.

5.1.1 *High equivalent width of the Hα broad component*

The BLR clouds absorb the ionizing continuum from the accretion disc and re-emit such radiation in the recombination nebular lines and continuum. In particular, the Hα luminosity is proportional to the luminosity of the ionizing photons, modulo the covering factor. This means that, if the intrinsic SED of AGN (from optical to UV ionizing bump) is the same, then the EW of the broad component of Hα should be a tracer of the covering factor of the BLR clouds.

Fig. 8 shows the distribution of the EW(H$\alpha_{\rm broad}$) for the type 1 AGN newly discovered at high-z by *JWST* (red histogram), compared with the same distribution for low-redshift AGN and quasars from the Sloan Digitalized Sky Survery (SDSS, blue histogram, Lusso et al. 2020). Clearly, the distribution of EW(H$\alpha_{\rm broad}$) of the high-z AGN found by *JWST* is shifted to much higher values relative to the low-redshift AGN. One should also take into consideration that in many of the AGN found by *JWST*, the optical continuum is contributed, and often dominated, by the stellar light from the host galaxy (Maiolino et al. 2024b, c; Juodžbalis et al. 2024a). Therefore, the EW estimated for the *JWST* galaxies are actually lower limits.

The vertical dashed lines in Fig. 8 indicate the medians of the two EW distributions, which are 200 Å for low-z AGN and quasars, while it is 570 Å for the high-z AGN identified by *JWST*. As mentioned above, the observed EWs are likely lower limits of the intrinsic EW, without galactic contamination. For this reason, the ratio between the two distributions is at least 2.6. If the covering factor of low-z, optically/UV-selected AGN was $\sim$40 per cent, then this ratio would imply that the BLR in the *JWST*-selected AGN would reach a covering factor of $\sim$100 per cent. However, as discussed above, the covering factor of the BLR in low-z, optically/UV-selected AGN is uncertain, with estimates ranging from 10 per cent to 50 per cent. So we can only quantitatively say that the covering factor of the *JWST*-selected AGN is at least a factor of 2.6 higher, on average.

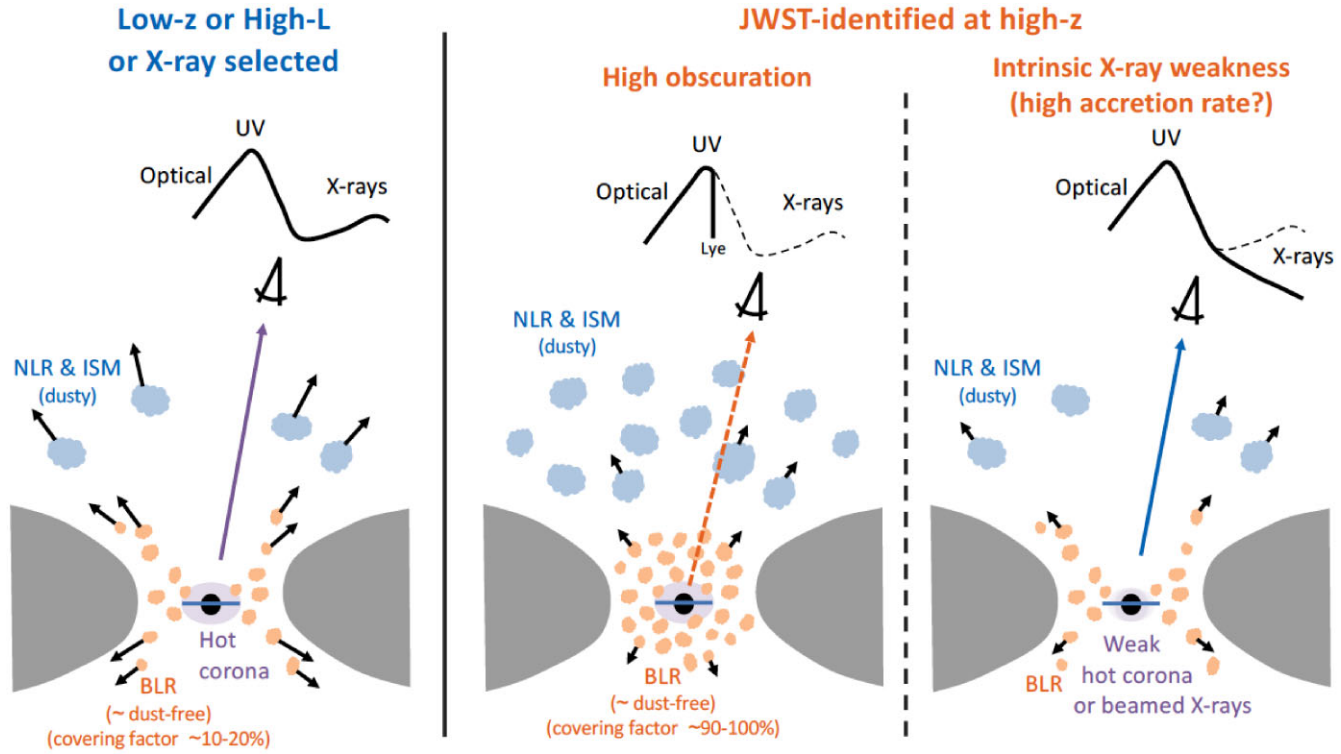

Figure 7. Sketch of possible scenarios illustrating the observed X-ray weakness of *JWST*-identified AGN at high-z as due to X-ray absorption from Compton-thick clouds with low dust content (possibly in the BLR, centre) and intrinsic X-ray weakness (right).

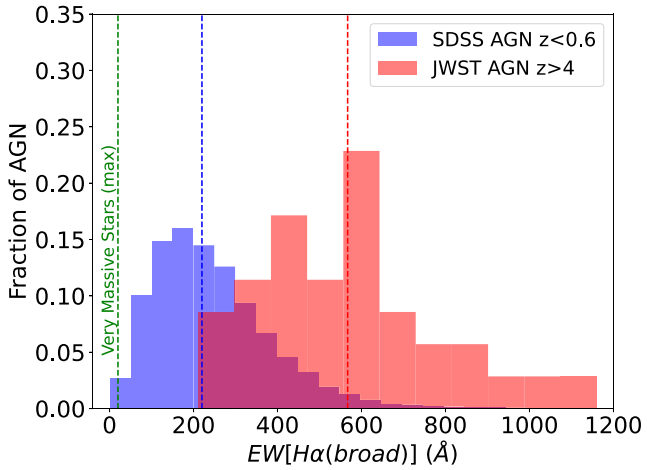

Figure 8. Distribution of the (rest-frame) EWs of the broad component of Hα for the AGN identified by *JWST* at high redshift (red) compared with AGN and quasars at low redshift (blue). The vertical red and blue dashed lines show the median of the two distributions. The vertical green dashed line indicate the maximum EW expected from VMSs.

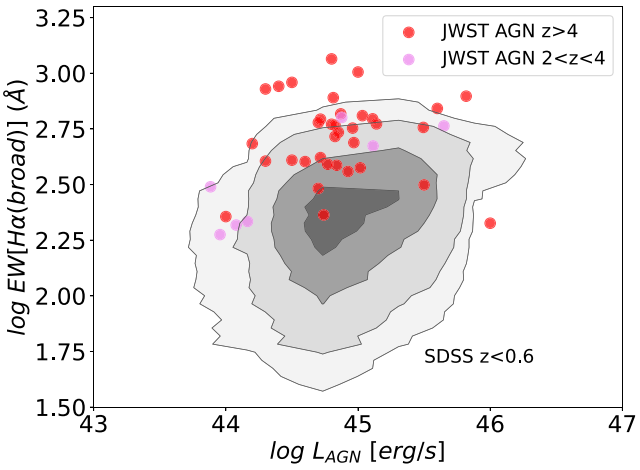

Figure 9. EW (rest-frame) of the broad component of Hα versus AGN bolometric luminosity, for the AGN identified by *JWST* at high redshift (red for those at $z>4$ and violet for those at $2<z<4$), compared with the distribution AGN and quasars at low redshift (grey contours).

As EW(H$\alpha_{\rm broad}$) has some dependence on AGN luminosity, in Fig. 9 we show the EW distribution as a function of $L_{\rm bol}$. Even when taking into account the dependence on $L_{\rm bol}$, the AGN found by *JWST* are significantly offset relative to standard AGN.

We have also tested the potential dependence on the accretion rate, in terms of $L/L_{\rm Edd}$. This is shown in Appendix B. Also in this case, the EW(H$\alpha_{\rm broad}$) is found to be larger than the distribution of optically selected AGN.

5.1.2 Additional indications of large gas columns and large absorbing densities

Out of the four X-ray-detected objects in our sample, the two detections that are deviating from the local $k_{\rm bol,X} - L_{\rm Bol}$ relation, i.e. XID403 at $z = 4.76$ GN 721 at $z = 2.94$, have X-ray spectra consistent with being Compton thick. Of the other three detections, GS 49729 ($z = 3.2$) and GS 209777 are not absorbed, but fully consistent with the local $k_{\rm bol,X} - L_{\rm Bol}$ relation, while GS 21150 (included in

the JADES sample because X-ray selected) is too faint to allow an estimate of the column density.

Outside the GOODS fields, the only X-ray AGN spectroscopically identified by *JWST* is UHZ-1, which is heavily Compton thick with $N_{\rm H} \sim 10^{25}$ cm^{-2} (Bogdan et al. 2024).

Kocevski et al. (2023) identified two additional AGN that were X-ray selected: PRIMER-COS 3982 at $z = 4.66$, which was however previously spectroscopically identified and confirmed from ground, and JADES 21925, which has a photometric redshift of $z = 3.1$, but not spectroscopically identified. In these two cases, the inferred column densities are substantial, $N_{\rm H} \sim 10^{23}$ cm^{-2}, although not Compton thick.

Taking into account that X-ray detections are biased against heavily obscured systems, it is remarkable that the two high-z X-ray AGN identified by *JWST*, for which spectral analysis was possible, are Compton thick. These might be the tip of the iceberg of a much larger population of Compton-thick AGN.

It is additionally interesting, among the *JWST*-discovered AGN, the emergence of type 1 AGN that show absorption features in the profiles of the broad Hα and/or Hβ. Absorption of the Balmer lines is extremely rare at low redshift, less than about 0.1 per cent of the AGN population (Zhang et al. 2015; Shi et al. 2016; Williams et al. 2017; Schulze et al. 2018). However, the *JWST* spectra are revealing an increasing number of these Balmer line absorption features in type 1 AGN. The AGN with the lower limit on $L_{\rm BOL}/L_X$ ($> 10^4$, Fig. 5) has prominent absorption of Hα and Hβ (Juodžbalis et al. 2024b). Matthee et al. (2024) found two cases of Hα absorption in their sample of 20 broad-line AGN, i.e. 10 per cent of their sample. Kocevski et al. (2024) find that 22 per cent of their broad-line AGN, hosted in little red dots, have some Hα in absorption. In the JADES spectroscopic data release, there are three type 1 AGN with Hα (and Hβ in one case) in absorption, out of a sample of about 30 type 1 AGN (Juodžbalis, in preparation; D'Eugenio et al. 2025). It should be noted that these fractions are lower limits, as detecting Hα or Hβ in absorption requires high S/N and, at least, medium-resolution spectroscopy ($R \sim 1000$) to disentangle the narrow- and broad-line emission profile from absorption. Those objects characterized by Balmer absorption are marked with magenta open circles in Fig. 5 and are indeed all extremely X-ray weak. As $n = 2$ is not a metastable level, observing Hα or Hβ in absorption requires, in addition to temperatures of $T \sim 1$–2×10^4 K, very large gas densities of $n > 10^9$ cm^{-3}, typical of the BLR (Williams et al. 2017; Juodžbalis et al. 2024b). Therefore, the unexpectedly high fraction of type 1 AGN with Hα or Hβ in absorption indicates that at least in 10 per cent of the cases we are likely seeing the optical continuum through BLR clouds, hence through a column of gas that is likely Compton thick. Note that detecting Balmer absorption is an extreme case that likely implies Compton thickness, while the opposite is not true: Compton-thick absorption does not necessarily imply Balmer absorption.

While the fraction of broad-line, type 1 AGN in the local/low-z Universe with Balmer absorption is very low, it is intriguing to note that the prototypical broad-line Seyfert 1 galaxy, NGC 4151, does show prominent Balmer absorption (Hutchings et al. 2002) and also strong (and variable) X-ray absorption, with absorbing column densities approaching 10^{24} cm^{-2} at times, resulting in significant X-ray weakness (Zoghbi, Miller & Cackett 2019). The location of NGC 4151 in Fig. 5 is shown with a light green diamond in a magenta circle.

We finally note that unobscured lines of sight passing through the BLR clouds should also result in absorption of the UV resonant lines, such as C IV, Si IV, and Al III. GN-z11 is one of these cases (Maiolino et al. 2024c), but there are very few other cases. However, most of the type 1 AGN identified by *JWST* show some degree of optical reddening ($A_V \sim 0.5 - 4$), which implies that, for most of them, the intrinsic UV radiation from the accretion disc is mostly absorbed. Therefore, the observed UV radiation is either dominated by stars in the host galaxies or scattered radiation, hence it would not be possible to see the UV absorption features associated with dense gas along the line of sight. Additionally, in order to be detected, the absorption features have to be shifted relative to the host galaxy rest frame, or else they would be filled in by the emission component of the same transition. If, as discussed, clouds linger in the nuclear region and do not have significant velocities, then they would be hard to see even at medium-/high-resolution spectroscopy, and impossible to see with prism spectroscopy. Finally, one should take into account that the blue part of the NIRSpec spectra has the lowest sensitivity and, typically, the noisiest. A number of potential absorption features are often seen, but difficult to validate with confidence.

5.1.3 *Low AGN ejective feedback*

One question is why the covering factor by dense gas (possibly from the BLR) should be much larger in the intermediate-luminosity AGN at high redshift discovered by *JWST*. One possibility is that the ejective feedback in these intermediate-luminosity AGN at high-z is much reduced, hence dense clouds linger in the vicinity of BHs. One indication going in this direction is that the population of AGN at high-z discovered by *JWST* seems to generally lack the prominent broad, blueshifted wings of [O III] tracing ionized outflows and typically seen in the vast majority of AGN at low-z, or at high-z, but with high luminosity or X-ray selected (Brusa et al. 2015; Carniani et al. 2015; Cresci et al. 2015; Bischetti et al. 2017; Leung et al. 2019; Kakkad et al. 2020).

We illustrate this property more quantitatively in Fig. 10, where we overplot the normalized and continuum subtracted [O III] profiles of different classes of AGN. The blue profiles show the [O III] doublet for AGN identified and selected before *JWST*. Specifically: the bottom-left plot shows the stack of AGN and quasars at z<0.6 from SDSS (Lusso et al. 2020, $R \sim 2000$), in a luminosity range $10^{44} < L_{\rm AGN} < 10^{45.5}$ erg s^{-1}, hence matching the type 1 luminosity range found with *JWST* by Maiolino et al. (2024b, details on the stacking procedure are given in Appendix C); the top-right plot shows plot shows the stack of the luminous SDSS quasars at $z \sim 6$ observed with *JWST* by Marshall et al. (2023), Eilers et al. (2023), and Loiacono et al. (2024, $R \sim 2000$–2700); the central plot shows the spectrum of XID2028, an X-ray-selected luminous AGN at $z = 1.5$, observed with *JWST* by Cresci et al. (2023) and Veilleux et al. (2023, $R \sim 2700$). The red lines show [O III] profiles of *JWST*-identified AGN (all X-ray undetected). Specifically: the bottom-right plot shows the stack of the high-resolution spectra ($R \sim 2700$) of the type 1 AGN in JADES presented in Maiolino et al. (2024b, $R \sim 2700$, note that high-resolution spectra are often unavailable for other NIRSpec MSA surveys, which often use only $R = 1000$ or even Prism); the central-line rightmost plot shows the spectrum of GS_3073, the X-ray undetected type 1.8 AGN identified by Übler et al. (2023, $R \sim 2700$) and previously discussed. Clearly, the AGN-selected pre-*JWST*, at low-z, or high-z but high luminosity, or X-ray selected, have a broader [O III] profile and, most importantly, a prominent [O III] blue wing, tracing high velocity ionized outflows. On the contrary, the X-ray undetected, *JWST*-identified AGN have narrower [O III] profiles and, most importantly, they lack the prominent blueshifted wings seen in other AGN. It should be noted that GS_3073 does have some very faint wings, actually redshifted, which in the IFS cube have been interpreted as an ionized weak outflow (Übler et al. 2023); however,

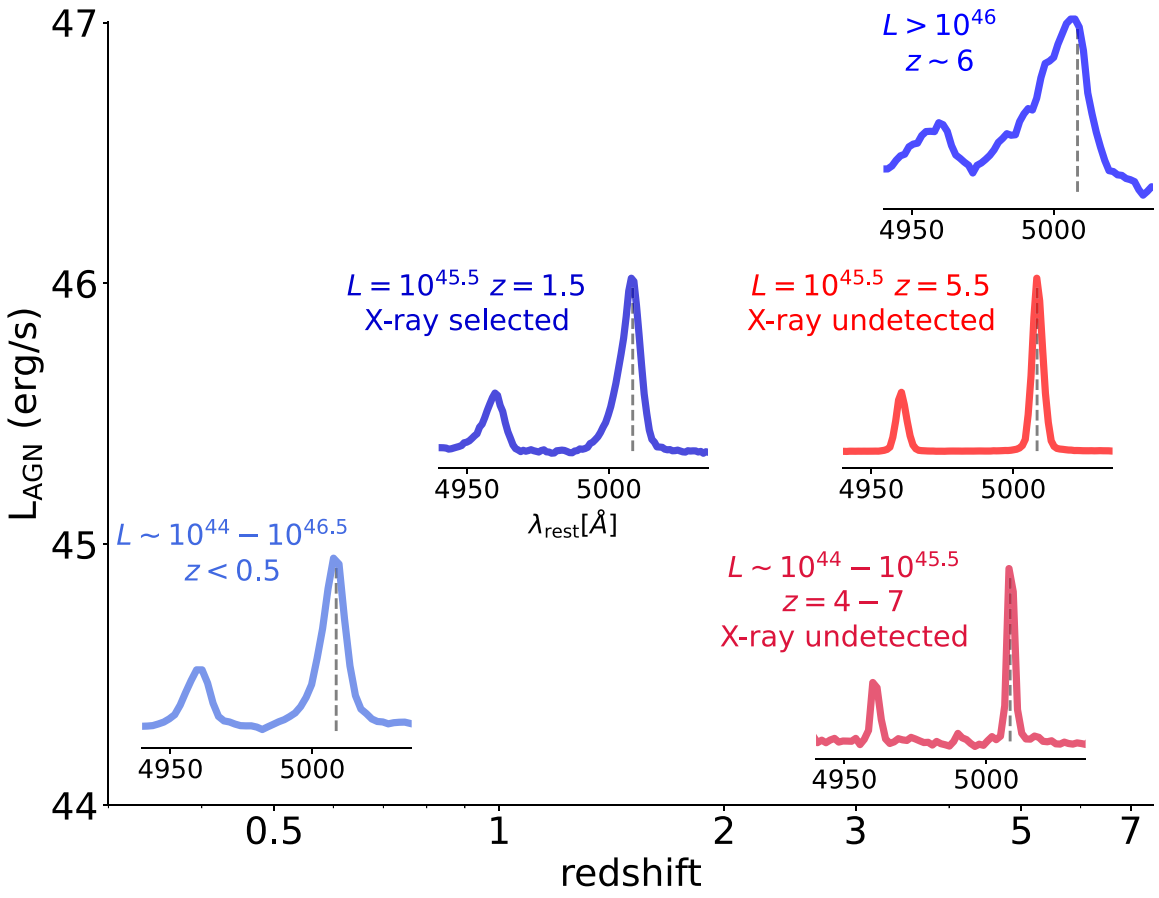

Figure 10. Comparison between the profiles of the [O III]5007 doublet for different classes of galaxies. The blue lines indicate pre-*JWST*-selected objects, specifically: stack of low-redshift AGN with intermediate luminosities, the X-ray-selected AGN XID2028 at $z = 1.5$, and stack of luminous (optically selected) quasars at $z > 6$ (see text for details). The red lines show some of the *JWST*-identified AGN: stack of the (X-ray undetected) JADES type 1 sample in Maiolino et al. (2024b) at $4 < z < 7$; spectrum of the type 1.8 GS_3073, X-ray undetected, AGN at $z = 5.5$. The high-luminosity, X-ray-selected and low-z AGN, have broader [O III] profiles and all have a prominent blue wing, typical signature of ionized outflows, while the AGN discovered by *JWST* at high-z have a narrow and symmetric profile, indicating much less prominent outflows, if any.

in terms of the ionized gas mass relative to the narrow component, it is far less prominent than in other AGN. The same applies to the stacked *JWST* type 1 spectrum: a very detailed and in depth analysis does reveal a very faint wing of [O III] (Trefoloni et al. 2024), but far weaker than seen in the stack of their low-redshift counterpart. Overall, the profile of the [O III] line suggests that the high-z AGN identified by *JWST* are driving very weak ionized winds, if any.

The large-scale ionized winds that are found in other AGN are thought to arise both from direct radiation pressure on dusty clouds and by energy-driven winds originating from the central region and involving the BLR (Fabian 2012; King & Pounds 2015; Costa et al. 2018; Costa, Pakmor & Springel 2020). The lack of ionized winds on large scales inferred from the [O III] symmetric profile suggests that also the BLR is characterized by weak winds. Directly identifying and characterizing winds of the BLR, or of gas distributed on similar scales, is more difficult. Typically, these are traced via the resonant UV lines, such as C IV. There is no evidence of C IV blueshifted absorption in any of the AGN analysed in our sample; yet, this may not be meaningful, as the UV light is generally dominated by the stellar light in the host galaxy (and see also the NIRSpec sensitivity issues in the bluest band discussed in the previous section). The only exception is GN-z11 at $z = 10.6$, which does show a clear C IV blueshifted absorption. The velocity ($\sim$ 800–1000 km s^{-1}) indicates that it is clearly driven by the AGN. However, it is far slower and shallower than typically seen in AGN and quasars with similar accretion rates (Maiolino et al. 2004; Gibson et al. 2009; Bischetti et al. 2022), indicating that even in this case the outflow is much milder than in other AGN. GS_3073 may also have a mild nuclear outflow traced by N V, but very weak (Ji et al. 2024).

The Hα absorption discussed above, seen with JWST in a few type 1 AGN of our sample, and most likely associated with absorption by BLR clouds along the line of sight, is blueshifted only by a few 100 km s^{-1} in three cases, redshifted in one case, and at rest frame in another case (Matthee et al. 2024; Juodžbalis et al. 2024b; D'Eugenio et al. 2025; Kocevski et al. 2024). Although these may not be representative of the entire sample, these direct tracers of the BLR kinematics, indicate that in these objects the BLR is either outflowing with very low velocities, stalling, or even inflowing.

In summary, the various lines of evidence support a scenario in which the ejective feedback in these *JWST*-selected AGN at high-z (which are the majority at high redshift) is less effective than for other classes of AGN studied in the past.

The reason why feedback is reduced in these low-/intermediate-luminosity AGN at high-z should be explored in detail in dedicated studies. We only speculate on the possibility that this could be due to the low metallicity characterizing these AGN at high-z. Wherever the

gas clouds are dusty, lower metallicity means lower dust content and, therefore, lower radiation pressure on dust. This should not affect the clouds in the BLR, which are dust-free. However, a reduced content of metals should also reduce the winds in the nuclear region, as these are primarily driven by line locking on the metal ionized species. At lower redshift, the higher metal enrichment and dust content are expected to foster outflows. Similarly, high-luminosity quasars probably manage to develop outflows even at high redshift, both because the radiation pressure is anyway very high and because they are hosted in more massive systems that have been enriched more rapidly, particularly in the nuclear region (Juarez et al. 2009; Costa et al. 2018, 2020; Ji et al. 2024).

Since these high-z galaxies are extremely compact and characterized by high gas densities (Tacchella et al. 2023; Ji et al. 2024), it could also be that the nuclear outflows struggle to develop to large scales and remain confined to the very central (pc-scale) region.

We note that ionized outflows have been detected in intermediate-luminosity AGN at $z\sim2$ (e.g. Förster Schreiber et al. 2014; Genzel et al. 2014) and neutral outflows have been identified in *JWST*-discovered AGN at $z\sim$2–3 (primarily via sodium absorption D'Eugenio et al. 2024; Belli et al. 2024; Davies et al. 2024). However, these are massive ($M_{\rm star} > 10^{10}$ M$_\odot$), metal-enriched galaxies, quite different from the bulk of the AGN population discovered by *JWST*, which are hosted in low-mass ($M_{\rm star} \sim 10^{8-10}$ M$_\odot$) and metal-poor host galaxies. Therefore, these are probably two different populations of AGN.

5.2 Intrinsically weak X-ray emission

Another possible factor contributing to the observed weakness of the X-ray emission can be the intrinsic weakness of the AGN emission. In this subsection, we investigate a few possible scenarios.

5.2.1 Narrow-line Seyfert 1 and high accretion rate

NLSy1 are defined as type 1 AGN whose 'broad' permitted lines have widths that are significantly narrower (FWHM $\sim$ 500–2000 km s^{-1}) than classic type 1 AGN and quasars, but still broader than the forbidden lines in the same objects (e.g. [O III]) (Osterbrock & Pogge 1985; Véron-Cetty, Véron & Gonçalves 2001; Berton et al. 2016). This class of AGN is thought to be characterized by high accretion rates, close to the Eddington limit, or even super-Eddington (Mathur 2000; Collin & Kawaguchi 2004). NLSy1 are well known to have a steeper X-ray spectrum than normal AGN, and this results in an X-ray weakness in the hard 2–10 keV band, by up to a factor of $\sim$5 (Vasudevan & Fabian 2007; Tortosa et al. 2022, 2023). Their softer spectrum is consistent with theoretical expectations that highly accreting AGN should have a softer ionizing spectrum. Some of the local NLSy1 are shown on the $L_{\rm bol}/L_{\rm X}$ versus $L_{\rm bol}$ diagram in Fig. 5 with purple diamonds, illustrating that some of them are indeed quite weaker than standard AGN in the 2–10 keV band.

Most of the AGN newly discovered by *JWST* are characterized by relatively narrow 'broad' permitted lines, and most of them are formally in the range of NLSy1. This is shown in Fig. 11, which provides the broad Hα FHWM distribution of the *JWST*-identified AGN at high-z, and indicates that many of them should be classified as NLSy1.

Additionally, a good fraction of the *JWST*-selected AGN have fairly high accretion rates, close to or even above the Eddington limit (Maiolino et al. 2024b). At low redshift, it has been shown that highly accreting BHs can be X-ray weak (Laurenti et al. 2022). Theoretically, it has been recently proposed that highly accreting BHs, possibly above the Eddington limit, should have their X-ray emission beamed in a narrow angle, hence X-ray weak along most of the lines of sight (Madau & Haardt 2024; Pacucci & Narayan 2024; King 2025).

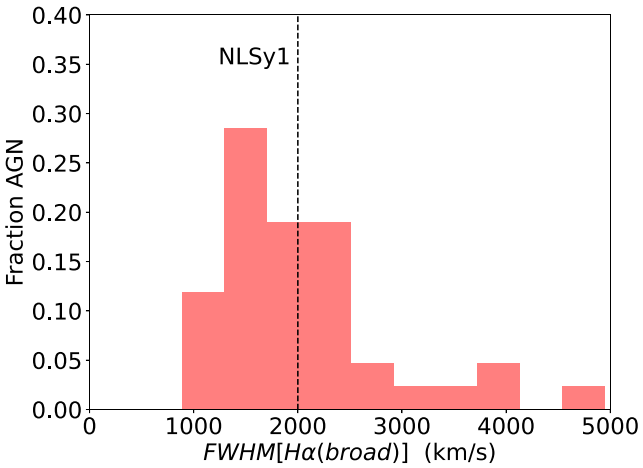

Figure 11. Distribution of the widths of the broad component of Hα among the type 1 AGN identified by *JWST* at high redshift. The vertical dashed line indicates the limit below which AGN are classified as NLSy1.

Therefore, it is very likely that part of the reasons why the *JWST* discovered AGN at high redshift are so X-ray weak may be associated with intrinsic weakness, as for local NLSy1 and highly accreting AGN.

Within this context, it is interesting to note that X-ray observations of high-z quasars do show evidence for a steeper spectrum, similar to local NLSy1 (Vito et al. 2019; Wolf et al. 2023; Zappacosta et al. 2023). This may suggest that a steep X-ray spectrum may be a common feature of AGN in the early Universe and that this may make them more difficult to detect them at high redshift (where we probe higher energies rest frame), unless the AGN has high, quasar-like luminosities.

However, as illustrated in Fig. 5, the similarity with NLSy1 cannot fully account for the X-ray weakness, especially the extremely high $L_{\rm bol}/L_{\rm X}$ seen in type 1 stacks and some individual cases. Additionally, there are examples of type 1 AGN identified by *JWST* that are clearly accreting well below the Eddington-limit and that are X-ray undetected, with $k_{\rm bol,X}$ more than one order of magnitude higher than the standard relations. The dormant BH GN-1146115 at $z = 6.67$ (Juodžbalis et al. 2024a), marked with a black solid circle in Fig. 5, is one of these cases.

Yet, although an X-ray soft, steep spectrum cannot fully account for the observed X-ray weakness, it can certainly contribute to making the observed X-ray emission undetected (Fig. 7), especially at high redshift, where we are probing the hard portion of the X-ray emission, possibly even with lower absorbing column, and relaxing the requirement of Compton thickness.

5.2.2 Reduced hot corona

Most models ascribe the production of hard X-rays to the inverse Compton scattering of the UV photons by a hot corona above the accretion disc (Haardt & Maraschi 1991). Therefore, one possibility is that these newly discovered AGN at high-z are lacking a hot corona, or that it is greatly reduced. Although intriguing, testing or even speculating on this possibility is difficult.

In the local Universe, there have been cases of destroyed corona (Ricci et al. 2020), but it is not clear what caused the event and, in particular, in these cases there is nothing obviously connected to the high-redshift Universe.

It is not clear how the hot corona is produced, but models expect that it should result from the magnetic field lifting material from the accretion disc. It could be that at high redshift, and around lower mass BHs, the magnetic field has not yet developed properly. As far as we are aware, there are no models or simulations describing the corona of AGN at high redshift and, in particular, in intermediate-luminosity AGN. Yet, there is recent major and very promising progress in the development of zoom-in radiation-magnetohydrodynamic simulations, down to very small scales (∼300 Schwarzschild's radii, Hopkins et al. 2024a, b; Koudmani et al. 2024; Martin-Alvarez et al. 2023). However, none of these simulations is yet probing the magnetic field in the accretion disc for BHs at high redshift in the mass range probed by our study.

5.3 Non-AGN contaminants

As discussed previously, most of the X-ray undetected AGN discovered by *JWST* have overwhelming and unambiguous evidence for the presence of AGN. The most spectacular case is GS_3073 that, in addition to the prominent broad permitted lines of the H Balmer series, H I and He II, also shows evidence for an array of 40 nebular emission lines, some of which coming from highly ionized species, and even coronal lines (N V, N IV, Ar IV, Fe VII, Fe XIII, and Fe XIV, Vanzella et al. 2010; Grazian et al. 2020; Übler et al. 2023; Ji et al. 2024), which unambiguously identify it as a luminous AGN. Despite that, it is undetected in the deepest region of the *Chandra* 7 Ms field. However, not all AGN identified by *JWST* have the same wealth of information. Yet, as discussed, the lack of X-ray emission is common to different AGN selection criteria (broad lines, narrow-line diagnostics, and mid-IR excess), and therefore it is unlikely that it arises from misclassification issues of all these methods. The lack of detection in the stacks would imply that the vast majority in each of those categories has been misclassified. In particular, in the case of type 1 AGN (which have the most stringent stacked constraint), the lower limit on $L_{\rm Bol}/L_{\rm X}$ inferred from the stack, which is more than two orders of magnitude above the value expected from the standard AGN SED, would imply that more than 99 per cent of the objects have been misclassified as AGN.

However, in the following, we discuss the scenario in which a fraction of the AGN identified by *JWST* might be misclassified.

5.3.1 Core-collapse supernovae

Core-collapse supernovae (cc-SNe) produce broad hydrogen emission lines which may potentially be mistaken for type 1 AGN. Yet, none of the type 1 AGN detected so far in the GOODS fields shows evidence for multi-epoch variability, indicating that individual SNe can be ruled out (e.g. Übler et al. 2024; Maiolino et al. 2024b; Juodžbalis et al. 2024a, DeCoursey et al. 2025). One potential issue is that in some cases the first epochs come from *Hubble Space Telescope* (*HST*), hence limited to wavelengths $< 1.8\,\mu$m. Therefore, obscured SNe may not be identified by *HST* imaging. However, several of the AGN found in the GOODS fields do have multi-epoch observations with NIRCam (DeCoursey et al. 2025), or by comparing IFS and NIRCam observations (Übler et al. 2024), and still do not show variability. Anyway, we also note that, even if some degree of variability was found, this could also be ascribed to AGN variability.

However, since the broad component of Hα can be bright even for 2–3 yr after explosion (Taddia et al. 2013; Fransson et al. 2014; Gutiérrez et al. 2017; Kokubo et al. 2019), it is possible that in some of the targets with broad Hα we are seeing the cumulative effect of multiple SNe. In this scenario, the SNe would be so frequent that their (photometric and broad-band) light curve would have to overlap in time to mimic the lack of variability. We have simulated this effect and, in order not to show variability at the level of 0.1 mag (sensitivity for variability), the galaxy should produce (in the photometric aperture) at least 10 SNe per year. This sets a lower limit on the star formation rate (SFR) of 500 $M_\odot\,yr^{-1}$. An upper limit on the SFR in the galaxies of our sample can be inferred by assuming the most conservative case that there is no AGN and that the observed Hα corrected for extinction is entirely produced by star formation. Fig. 12 shows the inferred distribution of (maximum) SFRs, together with the luminosity of the broad Hα; clearly, the maximum SFRs are well below the limit required by SN variability, indicated with a vertical dashed line (the region excluded by variability is indicated with grey shading). This comparison alone excludes significant contamination by cc-SNe, even in the scenario of cumulative, steady contribution.

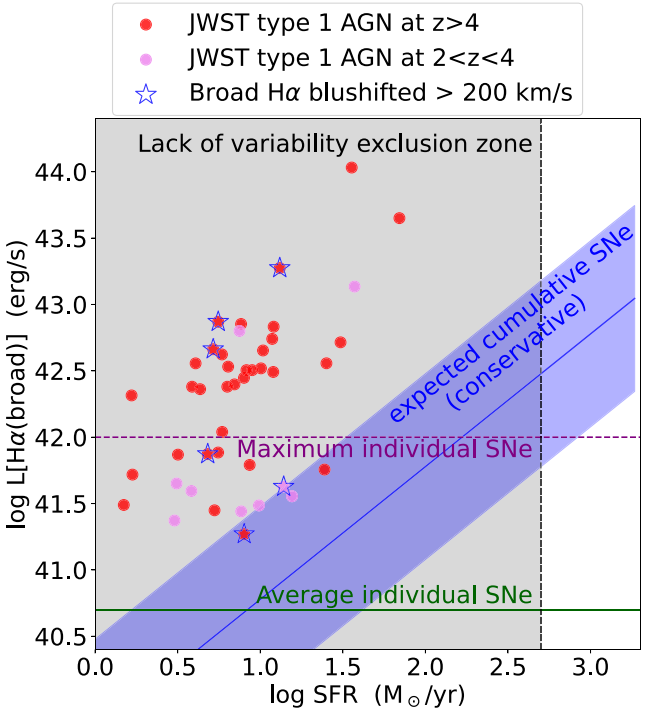

Figure 12. Constraints on the contribution cc-SNe to the broad component of Hα in a diagram showing the luminosity of the latter as a function of the SFR (derived assuming the extreme case that the narrow Hα is entirely due to star formation). Red and violet points indicate AGN identified by *JWST* at $z>4$ and at $2<z<4$, respectively. The vertical dashed line and grey shaded region show the region in which contribution from multiple SNe is excluded by the lack of variability. The blue solid line and blue shaded region indicate the expected contribution to the broad component of Hα from multiple SNe in the case continuous SFR. The horizontal green line shows the average broad Hα luminosity of cc-SNe, averaged over one year time-scale, as inferred from the samples in Kokubo et al. (2019) and Taddia et al. (2013). The horizontal purple dashed line shows the maximum luminosity of the broad component of Hα seen in rare, superluminous SNe. The open starred symbols indicate objects whose broad Hα is blueshifted by more than 200 km s^{-1}, as it is the case in the late phases of SN light curves.

Additionally, the solid blue line and blue shaded region in Fig. 12 indicate what would be the expected cumulative average luminosity of the broad component of Hα as a function of SFR (by conservatively

taking an average SN broad Hα luminosity of 10^{41} erg s^{-1} and, conservatively, over a time-scale of 3 yr, see Taddia et al. 2013; Kokubo et al. 2019), which is well below the value observed in the *JWST* type 1 AGN.

For completeness, we also show the maximum luminosity of the Hα broad line seen, at peak, in some rare superluminous SNe (Pastorello et al. 2002; Taddia et al. 2013; Fransson et al. 2014; Yan et al. 2015; Gutiérrez et al. 2017; Kokubo et al. 2019). We note however that the more typical peak luminosity is around 10^{41} erg s^{-1}. Hα luminosities of 10^{42} erg s^{-1} are much more rare and more short-lived than normal cc-SNe.

Finally, the SN interpretation is also problematic from the point of view of spectral properties. The broad component of Hα in SNe is generally very broad, often exceeding 10 000 km s^{-1} (Kokubo et al. 2019; Nicholl et al. 2019; Pessi et al. 2023), much broader than what is seen in most of the type 1 AGN identified by *JWST* (Fig. 11). In the early phases, Hα is generally characterized by a P-Cygni profile (Pastorello et al. 2002; Tartaglia et al. 2016; Gutiérrez et al. 2017; Dickinson et al. 2024) and at later times is generally blueshifted (Taddia et al. 2013; Fransson et al. 2014; Gutiérrez et al. 2017; Kokubo et al. 2019; Ransome et al. 2021), due to the formation of dust in the ejecta (Schneider & Maiolino 2024) – these properties are not observed in the type 1 AGN (although a few type 1 AGN in JADES do show blueshifted profiles, which will be discussed below). Additionally, the spectrum of cc-SNe is often also characterized by other prominent broad features, such as Mg I], Ca II, [O I], Fe II which are not seen in the *JWST* spectra (Taddia et al. 2013; Yan et al. 2015; Gutiérrez et al. 2017; Nicholl et al. 2019, 2020; Pessi et al. 2023). We note that none of these features is seen even in the stacked spectra of type 1 AGN (Trefoloni et al. 2024).

The only possibility to interpret some of the broad Hα emissions as associated with SNe in some of the objects, is to assume the case of an individual superluminous SN that exploded several months before the epoch of the observation, and which has faded below the threshold for being detected as a variable source, but whose broad Hα profile has remained visible on longer (few years) time-scales, and detectable for longer period, as seen in some cc (but not superluminous) SNe (Taddia et al. 2013; Fransson et al. 2014; Kokubo et al. 2019). This would require some more detailed modelling and fine tuning to identify the specific subclass of SN and the time frame in which the SN continuum variability would become undetectable (which is different from object to object) and the broad Hα still detectable. This is beyond the scope of this paper and will be addressed in a separate, dedicated work. Here we only note that such cc-SNe for which the broad Hα reaches the maximum luminosity ($\sim 10^{42}$ erg s^{-1}), hence most likely to be detected, are also those for which the broad Hα is short lived and has a steeper light curve, hence most difficult to fit in the scenario above. In the very dense gaseous environment typical of high-redshift galaxies, SNe are expected to release their energy even more rapidly, hence their features should also be more short lived. Additionally, we note that in the scenario above, in which the Hα broad is seen at late times, it should be seen significantly blueshifted (Taddia et al. 2013; Fransson et al. 2014; Gutiérrez et al. 2017; Kokubo et al. 2019; Ransome et al. 2021), due to the formation of dust in the SN ejecta (Schneider & Maiolino 2024). However, most of the Hα broad profiles are generally symmetric, possibly in some cases redshifted (Harikane et al. 2023; Matthee et al. 2024; Maiolino et al. 2024b; Übler et al. 2023, 2024; Juodžbalis et al. 2024a). There are only very few cases in which the broad Hα is blueshifted by more than 200 km s^{-1}, and these are marked with a blue star in Fig. 12. Out of these, three are well above the maximum Hα luminosity at the peaks of rare, superluminous SNe. Three are below this maximum value. We cannot exclude that these three (out of ∼44) could be associated with the echo of superluminous SNe.

In summary, significant contamination by cc-SNe to the population of type 1 AGN discovered by *JWST* is excluded on multiple grounds. However, a small fraction of the faintest type 1 AGN could be associated with the late echo of superluminous SNe.

We finally note that superluminous SNe are also observed to emit X-ray with luminosities above our detection threshold in stack (Levan et al. 2013; Greiner et al. 2015). This further confirms that they cannot account for the large population of type 1 AGN without X-ray emission.

5.3.2 *Very massive stars*

Young very massive stars (VMSs, $M_* > 100\,M_\odot$) are also characterized by a broad component of the Balmer lines (Martins et al. 2020, 2023). However, in these cases the EW of the broad component of Hα is very small, typically a few Å and always below 20 Å (Martins et al. 2020), i.e. much smaller than what observed in the *JWST* sources (green vertical dashed line in Fig. 8). It should be noted that the EW of the broad component of Hα expected from VMSs embedded in unresolved stellar populations is actually much lower, due to the dilution from the other, lower mass stars.

5.3.3 *Ionized galactic outflows*

It has been suggested that, in the case of type 1 AGN, the broad component of Hα is not tracing a BLR, and that it might be associated with fast outflows, with velocities of few thousands km s^{-1}, instead (Yue et al. 2024). However, in the case of SF-driven outflows the Hα broad wings reach values of only a few hundred km s^{-1} (e.g. Genzel et al. 2011), and not the thousands of km s^{-1} seen in our sample. More importantly, in the outflow scenario, such broad components should be seen even more prominently in the [O III] line. On the contrary, the [O III] profile does not show evidence for a broad component, which is not seen even in the stacked spectrum in Fig. 10. This excludes the outflow scenario with high confidence. The only possibility to suppress [O III], to the level of not being seen relative to the prominent Hα broad component, would be by assuming that the outflow has a metallicity below $10^{-2}\,Z_\odot$. This would be an order of magnitude lower than the metallicity of the host galaxies of these AGN (typically $0.1\,Z_\odot$) and would go in the opposite direction of what is observed in any other galactic outflows, whereby they are more metal enriched than the host galaxies that produce them.

5.3.4 *Tidal disruption events*

This class of events would not really be 'contaminants' as tidal disruption events (TDE) are effectively AGN, simply the source of fuel is different, stripped stars rather than gas from the circumnuclear region. Anyway, it is unlikely that this class of phenomena can contribute significantly. To begin with, TDE are known to show strongly variable light curves (Lodato & Rossi 2011; Gezari 2021), while, as mentioned in Section 5.3.1, there is no indication of variability. Secondly, more than 40 per cent of TDE emit strongly in X-rays, with luminosities $L_X > 10^{42}$ erg s^{-1} and up to $L_X \sim 10^{44}$ erg s^{-1} (Guolo et al. 2024), hence above our upper limits in several AGN. Finally, the Hα line profiles associated with TDEs (Gezari 2021) are typically significantly broader than observed in the *JWST*-identified type 1 AGN. Yet, it is possible, as for the case of superluminous SNe, that in a fraction of objects we are witnessing a phase in which the continuum variation is no longer detectable, but a broad Hα might

still be visible in the spectra. This is however difficult to test as the statistics on the temporal evolution of the broad Hα for TDE is less extensively studied than for SNe.

5.3.5 Type 2 contaminants

In the case of the type 2 AGN, none of the potential contaminants discussed above apply. However, since some of the classical diagnostics, such as the BPT, seem to break down at high redshift (Harikane et al. 2023; Maiolino et al. 2024b; Übler et al. 2023), searches for type 2 AGN have relied on alternative diagnostics. One of the most trustworthy is the detection of high ionization transitions, such as [Ne V], [Ne IV], and N V; however these are weak and detected only in a minority of objects (Scholtz et al. 2023; Chisholm et al. 2024). The majority of the type 2 selected by Scholtz et al. (2023) are identified either through a more restrictive version of the BPT diagrams (to minimize contamination by star forming galaxies with extreme conditions), or via diagnostic diagrams using UV transitions and based on photoionization modelling (Feltre, Charlot & Gutkin 2016; Nakajima & Maiolino 2022) (see also Mingozzi et al. 2024). While Scholtz et al. (2023) are very conservative in their type 2 selection, contamination by star-forming galaxies with extreme properties (high ionization parameter and harder ionizing spectra, for instance from WR stars) is still possible. However, since the stacked value of the $L_{\rm Bol}/L_{\rm X}$ for the type 2 sample is two orders of magnitude higher than expected from a standard AGN SED (and even larger if assuming the bolometric correction provided by Netzer 2019), this would imply that more than 99 per cent of the type 2 AGN have been misidentified. This is quite extreme, even because a number of them are confirmed by multiple diagnostics and some of them with very high ionization lines.

In summary, although a contamination of the type 2 AGN sample from extreme star-forming galaxies is possible, it is very unlikely that this can entirely explain the extreme X-ray faintness.

6 IMPLICATIONS

In this section, we discuss the implication of the X-ray weakness of the *JWST*-detected AGN, as well as the scenarios proposed, for our understanding of AGN properties and their evolution with cosmic time.

6.1 X-ray background

Padmanabhan & Loeb (2023) had pointed out that if the large population of AGN newly discovered by *JWST* shared the same standard SED as optically selected AGN (Shen et al. 2020), then they would overproduce the XRB by a large factor. However, we have unambiguously shown that the AGN discovered by *JWST* are much weaker in the X-rays than expected by the standard AGN SED. Regardless of the origin of the X-ray weakness, this indicates that this new population of AGN does not contribute to the XRB. The fact that a large population of high-z Compton-thick AGN could be accommodated without violating the XRB was already pointed out by Comastri et al. (2015).

6.2 AGN impact on early galaxy evolution

The finding of reduced AGN ejective feedback implies that galaxies in the early Universe suffer less of this negative effect on their evolution. This may allow galaxies to grow and form stars faster than predicted by previous models. Additionally, by removing less gas from the circumnuclear region and host galaxy, the lack of strong feedback would allow more fuel to reach the BH, which could grow more rapidly. This would help to explain the fast growth of BHs in the early Universe.

We finally note that, although the ejective feedback might be reduced, the accreting BHs probably still have significant feedback on their host galaxies in terms of heating, photodissociation, and photoionization of the interstellar medium.

6.3 Black hole masses

If the BLR has a covering factor much larger than previous studies, then this would imply that the local virial relations for estimating BH masses, and which use the luminosity of Hα as a proxy of the AGN bolometric luminosity (which enters in the equation for estimating the BH masses), should be revisited. In particular, the BH masses should be revised to lower values. However, the BH mass depends on the broad Hα luminosity only with a power of 1/2. Hence, if the covering factor of the BLR is higher by a factor between 2 and 10, relative to optical/UV-selected AGN (which have been used for the local calibrations), then the BH masses should be revisited downward by a factor between $\sim$1.4 and $\sim$3.

For the same reason, the bolometric luminosities inferred from the broad Hα would have been overestimated by a factor between 2 and 10. An implication of this is that the points on the $L_{\rm Bol}/L_{\rm X}$ versus $L_{\rm Bol}$ diagram (Fig. 5) would move along the diagonal, towards the bottom-left corner, by $\sim$0.3 dex and possibly up to 1 dex. This would bring some of the upper limits consistent with the local relation. However, many objects, and in particular the stack, would still deviate strongly even with the most extreme correction of 1 dex.

Finally, also the inferred accretion rates, in terms of $L/L_{\rm Edd}$, should also be lowered by a similar factor as for the BH masses, i.e. between $\sim$1.4 and $\sim$3.

6.4 Narrow-line region and diagnostic diagrams

If the BLR has a large covering factor, this would imply that only a small fraction of ionizing photons could escape to larger scales to ionize the NLR. If this is the case, then it would provide an additional explanation on why some of the classical narrow-line diagnostics fail to identify AGN at high redshift, as a significant fraction of the narrow lines would be dominated by star formation in the host galaxy, despite hosting a powerful AGN.

7 COMPARISON WITH PREVIOUS WORKS

X-ray weak AGN were obviously found also in the past. In the case of type 2 AGN, X-ray weakness has often been ascribed to heavy absorption, and generally directly confirmed with hard X-ray spectra, when the S/N was adequate (e.g. Salvati et al. 1997; Maiolino et al. 1998, 2003; Risaliti et al. 2000). Heavy obscuration in type 2 AGN, is therefore not surprising. What would be surprising, if the Compton-thick scenario is confirmed, is the large fraction of Compton-thick AGN. As we already mentioned, in the local Universe the fraction of Compton-thick AGN is about 50 per cent (Risaliti, Maiolino & Salvati 1999), while our findings indicate that the fraction of Compton-thick AGN might approach 100 per cent in high redshift, intermediate-/low-luminosity AGN. However, other studies have also found a significant evolution of the Compton-thick fraction, especially in the low-luminosity regime (Ananna et al. 2019; Gilli et al. 2022), although not as high as the one inferred by us. We notice, however, that selecting AGN via the broad Hα may bias towards AGN with high EW (Hα) and, therefore, those with high covering factor of the BLR. Yet, it remains true that, even if

biased, this population of AGN discovered by *JWST* is large in the early Universe, as evinced by the luminosity function presented by Maiolino et al. (2024b) for the same sample.

The other unexpected result is that type 1 AGN discovered by *JWST* are extremely X-ray weak too. This is much more unusual in the local Universe, or at high luminosities. Indeed, local type 1 AGN or optically/UV selected quasars at high redshift are characterized by prominent X-ray emission, although becoming gradually dimmer at the highest luminosities, as illustrated in Fig. 5. As mentioned, type 1 Broad Absorption Line (BAL) quasars are known to be X-ray weak and their weakness is associated with absorption (Gallagher et al. 2002, 2006), although some BAL quasars appear to be intrinsically weak (Luo et al. 2014; Teng et al. 2014). It is not clear if the type 1 AGN discovered by *JWST* at high-z are part of the BAL category. Exploring this scenario would require seeing directly the UV emission from the accretion disc, and exploring the presence of blueshifted UV resonant lines (e.g. C IV, S IV, and Al III). However, as already mentioned, most of them, although type 1 (actually they are generally type 1.5–1.9), show some dust reddening in the optical. This implies that the intrinsic UV emission is heavily suppressed and the host galaxy dominates the observed UV light. It is however interesting to note that GN-z11, the highest redshift type 1 AGN, does show C IV blueshifted absorption, similar to BAL quasars. Additionally, the presence of Balmer or He I absorption clearly indicates that these objects would appear as BAL quasars if observed in the UV without dust obscuration. Within this context, it is interesting to note that the fraction of (luminous) BAL quasars has been found to increase steeply at high redshift (Maiolino et al. 2001c, 2004; Bischetti et al. 2022).

Additionally, examples of X-ray weak type 1 quasars have been found in the past. Risaliti et al. (2001) explored the properties of emission line (grism) selected quasars and found that they are significantly X-ray weaker relative to the classical quasars selected via their blue colours. They ascribed the difference to dust-poor absorption along the line of sight, which suppresses the X-rays and only mildly redden their optical light.

Pu et al. (2020) also discovered a population of non-BAL X-ray weak quasars, although much smaller (∼5 per cent) than found among *JWST*-selected type 1 AGN. They found that a fraction of them tend to be reddened, in line with the absorption scenario. However, they also find that a fraction of them is characterized by weak broad emission lines. This result contrasts with the scenario where the BLR has a large covering factor. However, considering that these UV lines are heavily affected by even small amounts of dust, an absorption scenario may also apply. More recent observations of X-ray weak (type 1) quasars at high energies have revealed the emergence of a very hard component, indicating that their weakness is actually due to a dust-poor absorber with large (Compton thick) column density (Wang et al. 2022).

Interestingly, recent studies have also found that high-redshift sources are also significantly affected by X-ray absorption by the intergalactic medium (IGM, Arcodia et al. 2018; Dalton et al. 2022; Gatuzz et al. 2024), and that the absorbing column of gas increases quite steeply with redshift, as $(1+z)^{1.63}$. As the IGM is metal and dust poor, this is another possible source of X-ray weakness, without resulting in significant optical/UV obscuration. However, the IGM absorbing column densities inferred at $z\sim5$ are still of the order a few times 10^{22} cm^{-2}, not enough to explain the extreme X-ray weaknesses observed in our sample.

There are also several examples of type 1 X-ray weak AGN and quasars that are likely intrinsically weak, especially in the high accretion rate regime. As already mentioned, NLSy1, which are interpreted as highly accreting AGN, tend to be intrinsically X-ray weak (Vasudevan & Fabian 2007). Laurenti et al. (2022) analysed the X-ray properties of a sample of highly accreting quasars and found that they are intrinsically X-ray weak. X-ray weaknesses in highly accreting AGN is also expected from theoretical modelling (Valiante et al. 2018; Netzer 2019).

More recently, Paul et al. (2024) have identified a population of highly accreting AGN, which are X-ray weak. However, based on their radio properties, they suggest that the X-ray weakness is due to X-ray absorbing gas surrounding the accretion disc.

As already mentioned, the X-ray properties of type 1, *JWST*-selected AGN were already explored by Yue et al. (2024) and Ananna et al. (2024). However, they limited their analysis to a sample of so-called little red dots, which are only a small fraction (∼10 per cent–30 per cent) of the population of *JWST*-selected AGN at high redshift (Greene et al. 2024; Kocevski et al. 2024; Hainline et al. 2025). They suggest intrinsic X-ray weakness as a possible origin. Alternatively, they suggest that the broad component of Hα used to identify type 1 AGN might be due to fast galactic outflows (with velocities of a few thousand km s^{-1}). However, we have shown that the latter interpretation is untenable, as there is no evidence for such broad component in the forbidden lines (particularly [O III]), even in the stacked spectra.

Finally, we mention that Matsui et al. (2024) used X-ray stacking of *JWST*-selected galaxies at $4<z<7$ (expanding on a previous work at lower redshift, based on pre-*JWST* data, by Vito et al. 2016). From their non-detection they set an upper limit on the BH accretion rate density at high redshift. However, if in the intermediate-/low-luminosity range, high-z AGN are X-ray weak, then the global X-ray properties of high-z galaxies may not be very constraining of the bulk of BH accretion.

8 LOCAL ANALOGUES

Throughout the paper we have emphasized the 'peculiar' X-ray weakness of the intermediate-/low-luminosity AGN discovered by *JWST* at high-z. One may wonder why this property is found only at high redshift. However, AGN characterized by similar X-ray weakness have actually been found also locally, although possibly overlooked in the past. Leaving aside the large population of heavily absorbed (Compton-thick) narrow-line, type 2 AGN, there are also a growing number of broad-line, type 1 (or 1.9) AGN that are found to be X-ray weak, as discussed in the following.

We have already discussed the case of NGC 4151, the 'prototypical' broad-line, Seyfert 1 galaxy, which actually is heavily absorbed in the X-rays (Zoghbi et al. 2019), and also characterized by Balmer absorption (Hutchings et al. 2002), similar to several broad-line *JWST* AGN at high-z. We have also mentioned that the local population of highly accreting NLSy1 are also characterized by steep X-ray spectra, resulting in to X-ray weakness in the hard band that would be probed at high-z. However, there are also other local cases that are resembling the properties of *JWST*-identified AGN.

NGC 4151 is not the only case of type 1 AGN subject to high absorption in the X-rays. Studying an AGN sample selected from the *Swift* Burst Alert Telescope (BAT) , Shimizu et al. (2018) found a sample of type 1–1.9 AGN subject to significant X-ray absorption. As in our first interpretation, they suggest that BLR clouds might be responsible for X-ray absorption towards the corona. A similar finding, i.e. broad-lined AGN with prominent X-ray absorption, was obtained by Merloni et al. (2014) at intermediate redshifts.

Mrk231 is another remarkable local potential analogue, though it is likely representing a different category. This is the closest (type 1)

quasar and it is known to be extremely X-ray weak (Teng et al. 2014). Although moderately absorbed (by a partial covering medium), its X-ray weakness does not seem associated with absorption – it seems an intrinsic property. Teng et al. (2014) suggest that the X-ray weakness might originate from super-Eddington accretion.

Many more cases of type 1 AGN that are anomalously X-ray weak have been found among dwarf, low-metallicity galaxies, which may be more directly connected to the hosts of *JWST*-identified AGN at high-z. Simmonds et al. (2016) studied a sample of metal-poor galaxies candidate to host intermediate-mass BHs, based on their broad Hα, and found that they are X-ray undetected, with implied X-ray luminosity 1–2 orders of magnitude below the standard AGN UV-X-ray relations. A similar X-ray weakness was found by Burke et al. (2021) in a sample of broad-lined Hα, metal-poor dwarf galaxies. Interestingly, some of the galaxies analysed by Burke et al. (2021) are characterized by Hα absorption, as in *JWST*-selected AGN at high-z. Hatano et al. (2023) study in detail the very metal poor galaxy SBS 0335 and finding that not only it is characterized by a broad Hα (already found in previous studies; Izotov et al. 2009), but also variability in the mid-IR, hence unambiguously confirming the presence of an AGN. However, the nucleus is extremely weak in the X-ray, well below the expectation of a standard AGN SED, and the faint observed X-ray emission can be entirely ascribed to star formation in the host galaxy. Also in the case of SBS 3553 the high-resolution spectrum shows indication of Balmer absorption (Izotov et al. 2009), as in some of the high-z *JWST*-selected AGN.

Finally, Arcodia et al. (2024) explored the X-ray emission of a large sample of dwarf galaxies candidate to host AGN based on their optical/UV variability, and detected only a small minority of them. The stack of the several non-detected is much weaker than expected by the standard disc–corona relations for AGN. They suggest that a canonical X-ray corona might be missing in most of these AGN.

Summarizing, analogues of the X-ray weak AGN found by *JWST* at high-z are actually present in the local Universe, and they may have been overlooked. The connection between these local and distant populations needs to be explored in greater detail in future works. We however highlight that these potential local analogues provide an excellent (brighter) test bench to explore scenarios proposed for the distant populations.

9 CONCLUSIONS

We have leveraged the deepest *Chandra* observations in the GOODS fields to explore the X-ray properties of a large sample of 71 type 1 (broad line) and type 2 (narrow line) intermediate-luminosity AGN identified by *JWST* at $2<z<11$. These AGNs are identified from different parent samples and from different *JWST* surveys. However, they all have in common that they have typical luminosities significantly lower than those probed by previous (pre-*JWST*) surveys at high-z, and that they were not pre-selected because known to have an AGN based on previous observations at other wavelengths (with the exception of the two X-ray-selected objects). Additionally, these *JWST*-identified AGN are typically hosted in low-mass ($M_* \sim 10^8$–10^{10} M$_\odot$) and metal-poor ($Z \sim 0.1$ Z$_\odot$) host galaxies, in contrast with more luminous quasars at similar redshifts.

We have obtained the following results:

(i) The vast majority of AGN are undetected. For many of them, the X-ray upper limit is several times, up to two orders of magnitude, below what is expected from the standard SED of classical, optical/UV-selected AGN.

(ii) Only four objects are detected. Out of these, two were observed spectroscopically because of the previous X-ray detection. The X-ray spectrum of the two which are above the $L_{\rm bol}/L_{\rm X}$ standard relation reveals that they are Compton thick.

(iii) The type 1 AGN with evidence of absorption features in their Hα broad profile show some of the most extreme X-ray weaknesses.

(iv) The X-ray stacks of the non-detected AGN result in upper limits that are one to two orders of magnitude below what expected from standard AGN SED.

We explore the possible scenarios that can be at the origin of the X-ray weakness.

(1) *X-ray absorption*

(a) Absorption by large, Compton-thick columns of gas can explain the X-ray weakness.

(b) As the X-ray weakness is also seen in type 1 AGN (which are however typically reddened), this scenario implies absorption by a dust-poor (or dust-free) medium. The BLR clouds are a possible candidate (large column densities and dust-poor/free). However, the large fraction of X-ray weak AGN would imply a large covering factor of the BLR clouds.

(c) The EW(H$\alpha_{\rm broad}$) in *JWST*-identified AGN is much larger than in standard, optically/UV-selected AGN/quasars. This strongly supports the scenario of a BLR with a large covering factor.

(d) The finding of type 1 AGN with evidence of absorption features in their Hα broad profile also indicates absorption by gas with densities typical of the BLR.

(e) This scenario is further supported by the spectra of the few X-ray detected AGN above the $L_{\rm bol}/L_{\rm X}$ relation, which indeed reveal Compton thickness.

(f) The [O III]5007 line profile of *JWST*-identified AGN does not show the classical blueshifted wing seen in low-z AGN and high-luminosity quasars, indicating that ionized outflows in *JWST*-identified AGN are very weak. This suggests much reduced ejective feedback effects in the intermediate AGN luminosity, intermediate BH mass, and low-metallicity regime probed by *JWST*, and suggesting that the dense gas is lingering in the vicinity of the BH, causing the X-ray absorption.

(2) *Intrinsic X-ray weakness*

(a) Many of the AGN newly discovered by *JWST* are NLSy1s (i.e. with relatively narrow permitted lines, FWHM $<$ 2000 km s^{-1}, but still broader than the forbidden lines), which are known to have a very steep X-ray spectrum. This can contribute to their X-ray weakness, especially at high-z.

(b) Connected to the previous point, many *JWST*-identified AGN are accreting at high rates. Since higher BH accretion is expected to result into weaker X-ray emission, this can also contribute to the lack of detections. However, also dormant BHs are found to be very X-ray weak, implying that the accretion rate cannot be the only reason driving X-ray weakness.

(c) Another possibility, that is difficult to test, is that intermediate-mass BHs at high redshift have not yet developed properly their corona, possibly because the nuclear magnetic field is not yet strong enough.

(3) *Non-AGN sources*

(a) Given that the X-ray weakness is seen in the vast majority of *JWST*-identified AGN at high-z, regardless of their identification method (broad lines, narrow lines, and mid-IR

emission), it is highly unlikely that all of those selection methods have misidentifed AGN. The very stringent lower limits on the $L_{\rm Bol}/L_{\rm X}$ from the stacks would imply that more than 99 per cent of the sources have been misclassified. Additionally, a number of objects show widespread, multiple, and unambiguous AGN signatures (symmetric broad lines with very high EW, very high ionization lines) and, despite that, are still X-ray undetected.

(b) We have shown that cc-SNe cannot account for the observed broad Hα used to identify many type 1 AGN, based on multiple constraints (lack of significant variability, line luminosity, line profile, and absence of other spectral signatures). However, we have shown that a minority of the faintest broad Hα with blushifted profiles could be associated with the echoes of superluminous SNe.

(c) The contribution to the broad Hα by VMSs is excluded based on the very high EW of the line.

(d) TDEs would not be real contaminants, as they are anyway a form of AGN. They are however unlikely to contribute due to the lack of observed variability, the observed line profiles, and because many of them should also be detectable in the X-rays. However, we cannot exclude some minor contribution from this population.

(e) The contribution of galactic outflows is excluded by the lack of any broad component of [O III]5007, even in the stacked spectra.

(f) We do not exclude that a fraction of the type 2 AGN might actually be extreme star-forming galaxies. However, given that their stack results in a very stringent upper limit on their X-ray emission, it would imply that more than 99 per cent of them have been misclassified, which is unlikely given that for a good fraction of them the classification is confirmed by more than one diagnostic and/or show high ionization lines.

Probably, a combination of the scenarios discussed above is jointly responsible for the observed X-ray weaknesses. We stress that better discerning the role of each of these scenarios requires future X-ray observatories more sensitive than *Chandra*, such as the Advanced X-ray Imaging Satellite (AXIS) and the Advanced Telescope for High Energy Astrophysics (ATHENA) (Nandra et al. 2013; Marchesi et al. 2020; Reynolds et al. 2023).

Finally, we have also discussed some of the implications of the scenarios that emerged from our results.

(I) As the AGN identified by *JWST* are observed to be much X-ray weaker than expected by a standard AGN SED, their large number density is not in contrast with the XRB constraints.

(II) The lack of strong AGN-driven ejective feedback can have important implications on the early evolution of galaxies, allowing them to grow faster and also maintaining more gas available for rapid BH growth. However, heating and photodissociation feedback by the radiation produced by the AGN can still have an impact on the star formation efficiency.

(III) If the BLR covering factor is much larger than in the local AGN used to calibrate the BH virial relations, then this implies that the BH masses estimated in the *JWST*-identified AGN should be revisited downward by a factor of $\sim$1.4–3. For the same reason, the bolometric luminosities inferred from the broad Hα should be revisited downward by a factor of $\sim$2–10 and the accretion rates, in terms of $L/L_{\rm Edd}$, should also be revisited downward by a factor of $\sim$1.4–3.

(IV) Additionally, if the BLR covering factor is very large, this would leave few ionizing photons to escape the nuclear region and produce the narrow-line region. This may partly explain why the BPT diagrams of the *JWST*-selected AGN deviate from the locus populated by AGN locally.

ACKNOWLEDGEMENTS

RM, IJ, JS, HÜ, and FD and acknowledge support by the Science and Technology Facilities Council (STFC), by the European Research Council (ERC) through Advanced Grant 695671 'QUENCH', and by the United Kingdom Research and Innovation (UKRI) Frontier Research grant RISEandFALL. RM also acknowledges funding from a research professorship from the Royal Society. EB acknowledges financial support from INAF under the Large Grant 2022 'The metal circle: a new sharp view of the baryon cycle up to Cosmic Dawn with the latest generation IFU facilities'. HÜ gratefully acknowledges support by the Isaac Newton Trust and by the Kavli Foundation through a Newton-Kavli Junior Fellowship. MS acknowledges financial support from the Italian Ministry for University and Research, through the grant PNRR-M4C2-I1.1-PRIN 2022-PE9-SEAWIND: Super-Eddington Accretion: Wind, INflow and Disk-F53D23001250006-NextGenerationEU.

DATA AVAILABILITY

The X-ray data sets were obtained from the *Chandra* X-ray Centre https://cxc.harvard.edu/cda/ and *JWST* spectroscopic data are publicly available at MAST STScI archive https://archive.stsci.edu/missions-and-data/jwst.

REFERENCES

Alexander D. M. et al., 2003, AJ, 126, 539
Ananna T. T. et al., 2019, ApJ, 871, 240
Ananna T. T., Bogdán Á., Kovács O. E., Natarajan P., Hickox R. C., 2024, ApJ, 969, L18
Arcodia R. et al., 2024, A&A, 681, A97
Arcodia R., Campana S., Salvaterra R., Ghisellini G., 2018, A&A, 616, A170
Arnaud K. A., 1996, in Jacoby G. H., Barnes J., eds, ASP Conf. Ser. Vol. 101, Astronomical Data Analysis Software and Systems V, p. 17
Bassani L., Dadina M., Maiolino R., Salvati M., Risaliti G., Della Ceca R., Matt G., Zamorani G., 1999, ApJS, 121, 473
Belli S. et al., 2024, Nature, 630, 54
Bennett J. S., Sijacki D., Costa T., Laporte N., Witten C., 2024, MNRAS, 527, 1033
Berton M., Foschini L., Ciroi S., Cracco V., La Mura G., Di Mille F., Rafanelli P., 2016, A&A, 591, A88
Bischetti M. et al., 2017, A&A, 598, A122
Bischetti M. et al., 2022, Nature, 605, 244
Bogdan A. et al., 2024, Nat. Astron., 8, 126
Böker T. et al., 2022, A&A, 661, A82
Böker T. et al., 2023, PASP, 135, 038001
Brusa M. et al., 2015, A&A, 578, A11
Buchner J. et al., 2015, ApJ, 802, 89
Burke C. J., Liu X., Chen Y.-C., Shen Y., Guo H., 2021, MNRAS, 504, 543
Carniani S. et al., 2015, A&A, 580, A102
Chisholm J. et al., 2024, MNRAS, 534, 2633
Collin S., Kawaguchi T., 2004, A&A, 426, 797
Comastri A., Gilli R., Marconi A., Risaliti G., Salvati M., 2015, A&A, 574, L10
Costa T., Rosdahl J., Sijacki D., Haehnelt M. G., 2018, MNRAS, 473, 4197
Costa T., Pakmor R., Springel V., 2020, MNRAS, 497, 5229
Cresci G. et al., 2015, ApJ, 799, 82
Cresci G. et al., 2023, A&A, 672, A128
D'Eugenio F. et al., 2024, A&A, 689, A152
D'Eugenio F. et al., 2025, ApJS, 277, 4

Dalton T., Morris S. L., Fumagalli M., Gatuzz E., 2022, MNRAS, 513, 822
Davies R. L. et al., 2024, MNRAS, 528, 4976
DeCoursey C., et al. 2025. ApJ, 979, 250
Di Matteo T., Ni Y., Chen N., Croft R., Bird S., Pacucci F., Ricarte A., Tremmel M., 2023, MNRAS, 525, 1479
Dickinson D., Smith N., Andrews J. E., Milne P., Kilpatrick C. D., Milisavljevic D., 2024, MNRAS, 527, 7767
Duras F. et al., 2020, A&A, 636, A73
Eilers A.-C. et al., 2023, ApJ, 950, 68
Eisenstein D. J. et al., 2023, preprint (arXiv:2306.02465)
Elvis M., 2000, ApJ, 545, 63
Fabian A. C., 2012, ARA&A, 50, 455
Feltre A., Charlot S., Gutkin J., 2016, MNRAS, 456, 3354
Ferland G. J., Done C., Jin C., Landt H., Ward M. J., 2020, MNRAS, 494, 5917
Ferruit P. et al., 2022, A&A, 661, A81
Förster Schreiber N. M. et al., 2014, ApJ, 787, 38
Fransson C. et al., 2014, ApJ, 797, 118
Fruscione A. et al., 2006, in Silva D. R., Doxsey R. E., eds, Proc. SPIE Conf. Ser. Vol. 6270, Observatory Operations: Strategies, Processes, and Systems. SPIE, Bellingham, p. 62701V
Fujimoto S. et al., 2022, Nature, 604, 261
Furtak L. J. et al., 2024, Nature, 628, 57
Gallagher S. C., Brandt W. N., Chartas G., Garmire G. P., 2002, ApJ, 567, 37
Gallagher S. C., Brandt W. N., Chartas G., Priddey R., Garmire G. P., Sambruna R. M., 2006, ApJ, 644, 709
Gaskell C. M., Goosmann R. W., Antonucci R. R. J., Whysong D. H., 2004, ApJ, 616, 147
Gatuzz E., Wilms J., Hämmerich S., Arcodia R., 2024, A&A, 683, A213
Genzel R. et al., 2011, ApJ, 733, 101
Genzel R. et al., 2014, ApJ, 796, 7
Gezari S., 2021, ARA&A, 59, 21
Giallongo E. et al., 2019, ApJ, 884, 19
Gibson R. R. et al., 2009, ApJ, 692, 758
Gilli R. et al., 2011, ApJ, 730, L28
Gilli R. et al., 2022, A&A, 666, A17
Goulding A. D. et al., 2023, ApJ, 955, L24
Gravity Collaboration, 2018, Nature, 563, 657
Grazian A. et al., 2020, ApJ, 897, 94
Greene J. E. et al., 2024, ApJ, 964, 39
Greiner J. et al., 2015, Nature, 523, 189
Guo H. et al., 2020, ApJ, 888, 58
Guolo M., Gezari S., Yao Y., van Velzen S., Hammerstein E., Cenko S. B., Tokayer Y. M., 2024, ApJ, 966, 160
Gutiérrez C. P. et al., 2017, ApJ, 850, 89
Haardt F., Maraschi L., 1991, ApJ, 380, L51
Hainline K. N. et al., 2025, ApJ, 979, 138
Harikane Y. et al., 2023, ApJ, 959, 39
Hatano S. et al., 2023, preprint (arXiv:2304.03726)
Hopkins P. F. et al., 2024a, Open J. Astrophys., 7, 18
Hopkins P. F. et al., 2024b, Open J. Astrophys., 7, 19
Hutchings J. B., Crenshaw D. M., Kraemer S. B., Gabel J. R., Kaiser M. E., Weistrop D., Gull T. R., 2002, AJ, 124, 2543
Izotov Y. I., Guseva N. G., Fricke K. J., Papaderos P., 2009, A&A, 503, 61
Jakobsen P. et al., 2022, A&A, 661, A80
Jeon J., Bromm V., Liu B., Finkelstein S. L., 2025, ApJ, 979, 127
Ji X. et al., 2024, MNRAS, 535, 881
Juarez Y., Maiolino R., Mujica R., Pedani M., Marinoni S., Nagao T., Marconi A., Oliva E., 2009, A&A, 494, L25
Juodžbalis I. et al., 2024a, Nature, 636, 594
Juodžbalis I. et al., 2024b, MNRAS, 535, 853
Kakkad D. et al., 2020, A&A, 642, A147
King A., 2025, MNRAS, 536, L1
King A., Pounds K., 2015, ARA&A, 53, 115
Kocevski D. D. et al., 2023, ApJ, 954, L4
Kocevski D. D. et al., 2024, preprint (arXiv:2404.03576)
Kokorev V. et al., 2023, ApJ, 957, L7
Kokubo M. et al., 2019, ApJ, 872, 135
Koudmani S., Somerville R. S., Sijacki D., Bourne M. A., Jiang Y.-F., Profit K., 2024, MNRAS, 532, 60
Laurenti M. et al., 2022, A&A, 657, A57
Leung G. C. K. et al., 2019, ApJ, 886, 11
Levan A. J., Read A. M., Metzger B. D., Wheatley P. J., Tanvir N. R., 2013, ApJ, 771, 136
Li J. et al., 2025, ApJ, 981, 19
Lodato G., Rossi E. M., 2011, MNRAS, 410, 359
Loiacono F. et al., 2024, A&A, 685, A121
Luo B. et al., 2014, ApJ, 794, 70
Luo B. et al., 2017, ApJS, 228, 2
Lupi A., Quadri G., Volonteri M., Colpi M., Regan J. A., 2024, A&A, 686, A256
Lusso E. et al., 2020, A&A, 642, A150
Lyu J. et al., 2024, ApJ, 966, 229
Ma Y., Goulding A., Greene J. E., Zakamska N. L., Wylezalek D., Jiang Y.-F., 2024, ApJ, 974, 225
Madau P., Haardt F., 2024, ApJ, 976, L24
Maiolino R., Salvati M., Bassani L., Dadina M., della Ceca R., Matt G., Risaliti G., Zamorani G., 1998, A&A, 338, 781
Maiolino R., Marconi A., Salvati M., Risaliti G., Severgnini P., Oliva E., La Franca F., Vanzi L., 2001a, A&A, 365, 28
Maiolino R., Marconi A., Oliva E., 2001b, A&A, 365, 37
Maiolino R., Mannucci F., Baffa C., Gennari S., Oliva E., 2001c, A&A, 372, L5
Maiolino R., Salvati M., Marconi A., Antonucci R. R. J., 2001d, A&A, 375, 25
Maiolino R. et al., 2003, MNRAS, 344, L59
Maiolino R., Oliva E., Ghinassi F., Pedani M., Mannucci F., Mujica R., Juarez Y., 2004, A&A, 420, 889
Maiolino R. et al., 2010, A&A, 517, A47
Maiolino R. et al., 2024a, A&A, 687, A67
Maiolino R. et al., 2024b, A&A, 691, A145
Maiolino R. et al., 2024c, Nature, 627, 59
Mannucci F., Salvati M., Stanga R. M., 1992, ApJ, 394, 98
Marchesi S. et al., 2020, A&A, 642, A184
Marshall M. A. et al., 2023, A&A, 678, A191
Martin-Alvarez S., Sijacki D., Haehnelt M. G., Farcy M., Dubois Y., Belokurov V., Rosdahl J., Lopez-Rodriguez E., 2023, MNRAS, 525, 3806
Martins F., Schaerer D., Haemmerlé L., Charbonnel C., 2020, A&A, 633, A9
Martins F., Schaerer D., Marques-Chaves R., Upadhyaya A., 2023, A&A, 678, A159
Mathur S., 2000, MNRAS, 314, L17
Matsui S., Shimasaku K., Ito K., Ando M., Tanaka T. S., 2024, MNRAS, 529, 926
Matthee J. et al., 2024, ApJ, 963, 129
Mazzolari G. et al., 2024, A&A, 691, A345
Merloni A. et al., 2014, MNRAS, 437, 3550
Mingozzi M. et al., 2024, ApJ, 962, 95
Moretti A., Campana S., Lazzati D., Tagliaferri G., 2003, ApJ, 588, 696
Nakajima K., Maiolino R., 2022, MNRAS, 513, 5134
Nandra K. et al., 2013, preprint (arXiv:1306.2307)
Nardini E., Risaliti G., 2011, MNRAS, 417, 2571
Natarajan P., Pacucci F., Ricarte A., Bogdán Á., Goulding A. D., Cappelluti N., 2024, ApJ, 960, L1
Netzer H., 1990, in Blandford R. D., Netzer H., Woltjer L., Courvoisier T. J. L., Mayor M., eds, Active Galactic Nuclei. Springer Berlin, Heidelberg, p. 57
Netzer H., 2019, MNRAS, 488, 5185
Nicholl M., Berger E., Blanchard P. K., Gomez S., Chornock R., 2019, ApJ, 871, 102
Nicholl M. et al., 2020, Nat. Astron., 4, 893
Niida M. et al., 2020, ApJ, 904, 89
Oesch P. A. et al., 2023, MNRAS, 525, 2864
Osterbrock D. E., Pogge R. W., 1985, ApJ, 297, 166
Pacucci F., Narayan R., 2024, ApJ, 976, 96
Pacucci F., Nguyen B., Carniani S., Maiolino R., Fan X., 2023, ApJ, 957, L3
Padmanabhan H., Loeb A., 2023, ApJ, 958, L7

Pancoast A. et al., 2018, ApJ, 856, 108
Parlanti E. et al., 2024, A&A, 684, A24
Pastorello A. et al., 2002, MNRAS, 333, 27
Paul J. D. et al., 2024, ApJ, 974, 66
Peca A. et al., 2023, ApJ, 943, 162
Perna M. et al., 2023, preprint (arXiv:2310.03067)
Pessi P. J. et al., 2023, MNRAS, 523, 5315
Peterson B. M., 2006, in Alloin D., ed., Physics of Active Galactic Nuclei at all Scales, Vol. 693. Springer, Berlin and Heidelberg, p. 77
Planck Collaboration VI, 2020, A&A, 641, A6
Pu X., Luo B., Brandt W. N., Timlin J. D., Liu H., Ni Q., Wu J., 2020, ApJ, 900, 141
Ransome C. L., Habergham-Mawson S. M., Darnley M. J., James P. A., Filippenko A. V., Schlegel E. M., 2021, MNRAS, 506, 4715
Rantala A., Naab T., Lahén N., 2024, MNRAS, 531, 3770
Reynolds C. S. et al., 2023, in Siegmund O. H., Hoadley K., eds, Proc. SPIE Conf. Ser. Vol. 12678, UV, X-Ray, and Gamma-Ray Space Instrumentation for Astronomy XXIII. SPIE, Bellingham, p. 126781E
Ricci C. et al., 2020, ApJ, 898, L1
Risaliti G., Maiolino R., Salvati M., 1999, ApJ, 522, 157
Risaliti G., Gilli R., Maiolino R., Salvati M., 2000, A&A, 357, 13
Risaliti G., Marconi A., Maiolino R., Salvati M., Severgnini P., 2001, A&A, 371, 37
Risaliti G., Elvis M., Nicastro F., 2002, ApJ, 571, 234
Risaliti G., Elvis M., Fabbiano G., Baldi A., Zezas A., 2005, ApJ, 623, L93
Risaliti G., Nardini E., Salvati M., Elvis M., Fabbiano G., Maiolino R., Pietrini P., Torricelli-Ciamponi G., 2011, MNRAS, 410, 1027
Salvati M., Bassani L., della Ceca R., Maiolino R., Matt G., Zamorani G., 1997, A&A, 323, L1
Schneider R., Maiolino R., 2024, A&AR, 32, 2
Schneider R., Valiante R., Trinca A., Graziani L., Volonteri M., Maiolino R., 2023, MNRAS, 526, 3250
Scholtz J. et al., 2023, preprint (arXiv:2311.18731)
Scholtz J. et al., 2024, A&A, 687, A283
Schulze A., Misawa T., Zuo W., Wu X.-B., 2018, ApJ, 853, 167
Scoggins M. T., Haiman Z., Wise J. H., 2023, MNRAS, 519, 2155
Shen X., Hopkins P. F., Faucher-Giguère C.-A., Alexander D. M., Richards G. T., Ross N. P., Hickox R. C., 2020, MNRAS, 495, 3252
Shi X. et al., 2016, ApJ, 819, 99
Shimizu T. T. et al., 2018, ApJ, 856, 154
Signorini M. et al., 2023, A&A, 676, A49
Simmonds C., Bauer F. E., Thuan T. X., Izotov Y. I., Stern D., Harrison F. A., 2016, A&A, 596, A64
Stern J., Laor A., 2012, MNRAS, 423, 600
Tacchella S. et al., 2023, ApJ, 952, 74
Tacchella S. et al., 2024, preprint (arXiv:2404.02194)
Taddia F. et al., 2013, A&A, 555, A10
Tartaglia L. et al., 2016, ApJ, 823, L23
Teng S. H. et al., 2014, ApJ, 785, 19
Tortosa A. et al., 2022, MNRAS, 509, 3599
Tortosa A. et al., 2023, MNRAS, 519, 6267
Trefoloni B. et al., 2024, preprint (arXiv:2410.21867)
Tremmel M., Ricarte A., Natarajan P., Bellovary J., Sharma R., Quinn T. R., 2024, Open J. Astrophys., 7, 26
Trinca A., Schneider R., Maiolino R., Valiante R., Graziani L., Volonteri M., 2023, MNRAS, 519, 4753
Übler H. et al., 2023, A&A, 677, A145
Übler H. et al., 2024, MNRAS, 531, 355
Valiante R., Schneider R., Zappacosta L., Graziani L., Pezzulli E., Volonteri M., 2018, MNRAS, 476, 407
Vanzella E. et al., 2010, A&A, 513, A20
Vasudevan R. V., Fabian A. C., 2007, MNRAS, 381, 1235
Veilleux S. et al., 2023, ApJ, 953, 56
Véron-Cetty M. P., Véron P., Gonçalves A. C., 2001, A&A, 372, 730
Vito F. et al., 2016, MNRAS, 463, 348
Vito F. et al., 2019, A&A, 630, A118
Volonteri M., Habouzit M., Colpi M., 2023, MNRAS, 521, 241
Wang C. et al., 2022, ApJ, 936, 95
Williams R. J., Maiolino R., Krongold Y., Carniani S., Cresci G., Mannucci F., Marconi A., 2017, MNRAS, 467, 3399
Wolf J. et al., 2023, A&A, 669, A127
Xue Y. Q., Luo B., Brandt W. N., Alexander D. M., Bauer F. E., Lehmer B. D., Yang G., 2016, ApJS, 224, 15
Yan L. et al., 2015, ApJ, 814, 108
Yue M., Eilers A.-C., Annana T. T., Panagiotou C., Kara E., Miyaji T., 2024, ApJ, 974, L26
Zappacosta L. et al., 2023, A&A, 678, A201
Zhang S. et al., 2015, ApJ, 815, 113
Zhang H., Behroozi P., Volonteri M., Silk J., Fan X., Hopkins P. F., Yang J., Aird J., 2023, MNRAS, 518, 2123
Zoghbi A., Miller J. M., Cackett E., 2019, ApJ, 884, 26

APPENDIX A: X-RAY SPECTRA OF DETECTIONS AND STACKS

In this appendix, we show the spectra of the two detected sources (Fig. A1) and of the stacked spectra of the two luminosity bin $\log(L_{\rm BOL}) < 44.9$ and $\log(L_{\rm BOL}) > 44.9$ for the type 1 AGN at $z > 4$ (Fig. A2).

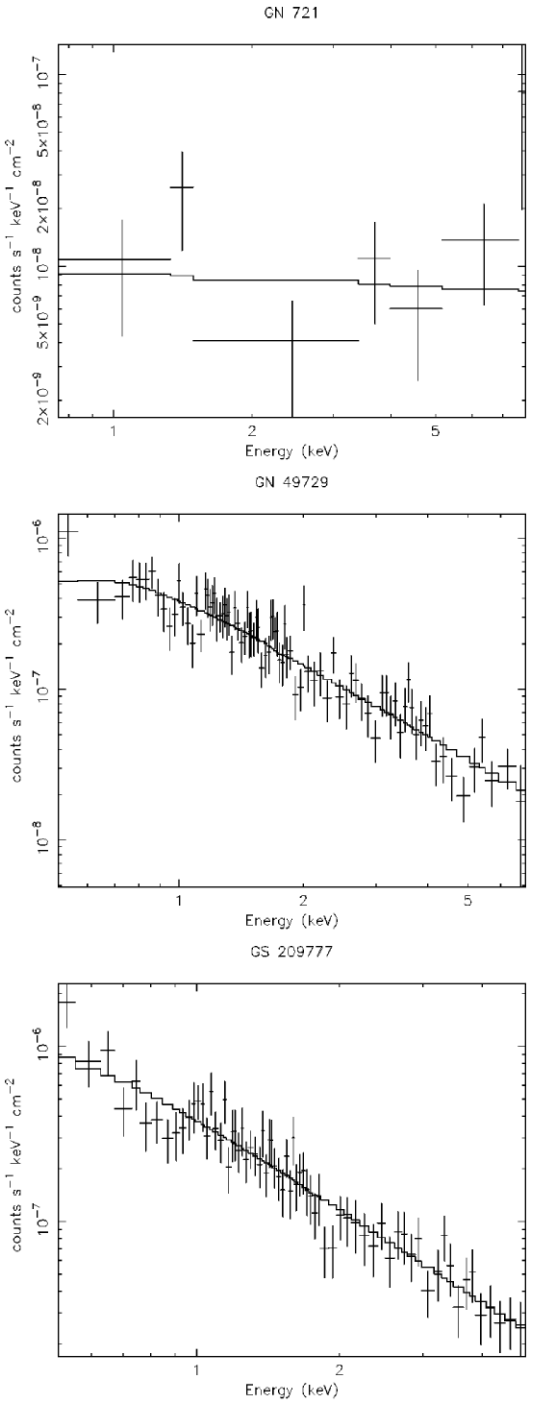

Figure A1. Spectra of the three detected objects: GN 721 (top panel), GS 49729 (middle panel), and GN 209777 (bottom panel). The low S/N detection of GN 721 only allows a rough estimate of the photon index $\Gamma = 0.1 \pm 0.6$, suggesting a reflection-dominated spectrum (hence a spectrum in which the direct component is likely completely absorbed by a Compton-thick medium). The spectrum of GS 49729 is reproduced by a power law with $\Gamma = 1.6 \pm 0.05$ and absorbing column density $N_H < 4 \times 10^{22}$ erg cm^{-1}s^{-2}. Similarly, the spectrum of GS 209777 is reproduced by a power law with $\Gamma = 1.7 \pm 0.1$ and absorbing column density $N_H < 3 \times 10^{22}$ erg cm^{-1}s^{-2}.

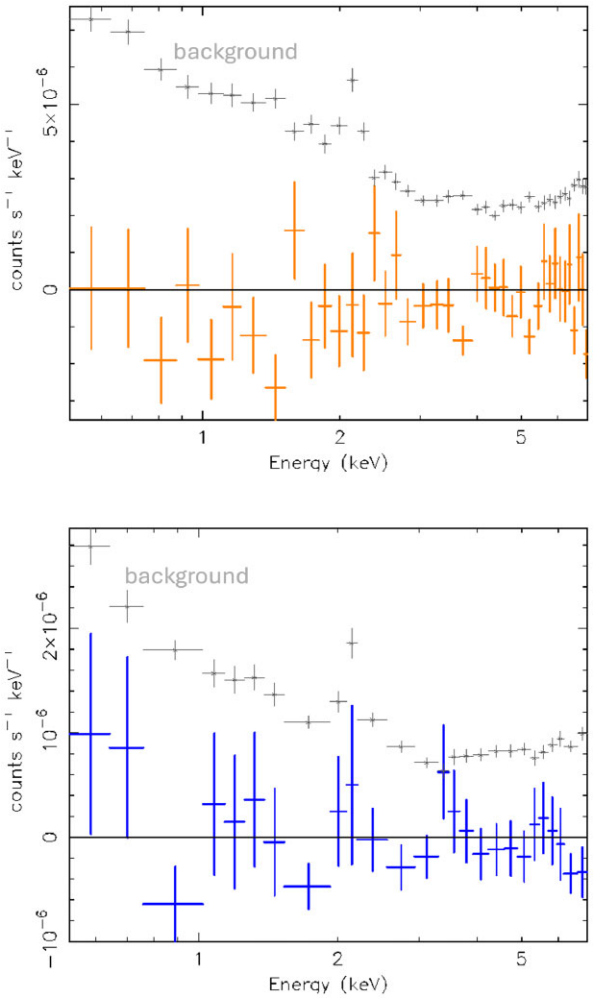

Figure A2. Stacked X-ray spectra for the high-luminosity (top panel) and low-luminosity (bottom panel) type 1 subsamples at $z > 4$. The grey points show the background level. In both cases, the stacked spectra are consistent with zero net counts, and are well below the background level.

APPENDIX B: EW(Hα) VERSUS ACCRETION RATE

Fig. B1 shows the distribution of EW(H$\alpha_{\rm broad}$) as a function of accretion rate, $L/L_{\rm Edd}$. The grey-shaded contours show the distribution of AGN and quasars at low redshift, from Lusso et al. (2020). The circles show the distribution of *JWST*-discovered AGN, red for those at $z > 4$ and violet for those at $2 < z < 4$. The local distribution does not show any significant correlation, as already pointed out by Ferland et al. (2020). The *JWST*-identified AGN are, on average, located above the local distribution, regardless of $L/L_{\rm Edd}$.

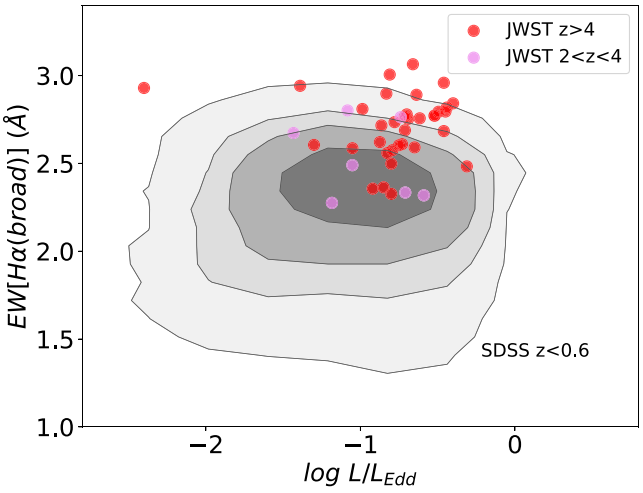

Figure B1. EW of the broad component of Hα versus AGN accretion rate, $L/L_{\rm Edd}$, for the AGN discovered by *JWST* at high redshift (red for those at $z > 4$ and violet for those at $2<z<4$), compared with AGN and quasars at low redshift (grey contours).

APPENDIX C: OPTICAL AND INFRARED SPECTRA STACKING METHODOLOGY

In this appendix, we provide additional information on the stacking procedure for the optical (SDSS) and near-IR (JWST) spectra around [OIII]. All spectra were shifted to rest frame and rebinned to a common wavelength grid, designed so as to preserve the observed frame resolution also in the rest frame. The spectra are then normalized by their flux at a reference wavelength (generally 5100 Å) in order not to bias the stack towards the most luminous objects. In each spectral channel, a bootstrap procedure was adopted to evaluate both the average flux and the uncertainty. In brief, a target number of average spectra is decided before the stacking (generally $N_{\rm target} = 100$). Then, $N_{\rm draw}$ spectra, with $N_{\rm draw}$ equal to the total number of spectra in each sample, are randomly extracted allowing for replacement and stacked together taking the median flux in each spectral channel (less prone to extreme values) to create the ith composite spectrum. This procedure was performed $N_{\rm target}$ times, building the distribution of the mean fluxes in each spectral channel. The final spectrum in each spectral channel was obtained as the mean of the mean fluxes and the uncertainty as the standard deviation.

This paper has been typeset from a TEX/LATEX file prepared by the author.